MSc thesis in Applied Earth Sciences

Simulation of CO2 Storage in Complex Geological Formations Using Parameterized Physics Spaces

Ziliang Zhang

August 2022

A thesis submitted to the Delft University of Technology in partial fulfillment of the requirements for the degree of Master of Applied Earth Sciences

TU Delft

Author

Ziliang Zhang — MSc Student, Geo-Energy Engineering
Department of Geosciences and Engineering
Delft University of Technology

Thesis committee

Dr. Hadi Hajibeygi — Supervisor, Associate Professor
Department of Geosciences and Engineering
Delft University of Technology

Dr. Yuhang Wang — Co-supervisor, Postdoc
Department of Applied Mathematics
Delft University of Technology

Prof. Cornelis Vuik — Committee, Professor
Department of Applied Mathematics
Delft University of Technology

Dr. Maartje Boon — Committee, Postdoc
Department of Geosciences and Engineering
Delft University of Technology

Ziliang Zhang: *Simulation of CO2 Storage in Complex Geological Formations Using Parameterized Physics Spaces* (2022)

The work in this thesis was carried out in the:

DARSim
Delft Advanced Reservoir Simulation

Delft Advanced Reservoir Simulation
Delft University of Technology

Abstract

In this work, an efficient compositional framework is developed to simulate CO2 storage in saline aquifers with complex geological geometries during a lifelong injection and migration process. The novelty of the development is that essential physics for CO2 trapping are considered by a parametrization method.

The numerical framework considers essential hydrodynamic physics, including hysteresis, dissolution and capillarity, by means of parameterized space to improve the computation efficiency. Those essential trapping physics are translated into parameterized spaces during an offline stage before simulation starts. Among them, the hysteresis behavior of constitutive relations is captured by the surfaces created from bounding and scanning curves, on which relative permeability and capillarity pressure are determined directly with a pair of saturation and turning point values.

On the other hand, the new development allows for simulation of realistic reservoir models with complex geological features by implementing in corner point gird. The extension to corner point grid is validated by comparing simulation results obtained from the cartesian-box and the converted corner-point grid of the same geometry, and it is applied to a field-scale reservoir eventually.

A set of sensitivity analysis reveals the roles of various physical effects and their interactions in CO2 trapping in a realistic reservoir model, apart from the investigation on the impact of migration path, linear trapping coefficient and depth. The results show the proposed compositional framework casts a promising approach to predict the migration of CO2 plume, and to assess the amount of CO2 trapped by different trapping mechanisms in realistic field-scale reservoirs.

Acknowledgements

At the time preparing the thesis, it comes to an end of my master study period at Delft University of Technology. When looking back to this fulfilling journey, I would like to express my thanks to some people who make it happen.

Firstly, I would like to express the deepest appreciation to my supervisor, Dr. Hadi Hajibeygi, for the motivation and support. I still can remember a lot of inspiring moments from your lectures, never to mention your patience and willingness to help during project meetings. Your enthusiasms towards the project would always remind me how meaningful and interesting the research work is.

Next, words cannot express my gratitude to Dr. Yuhang Wang who guided me throughout this project. I would never forget that you have always been there when I want to discuss with you, or share the exciting moments while having breakthrough. Meetings are always not long enough to learn the expertise of knowledge from you.

I appreciate, Prof. Kees Vuik and Dr. Maartje Boon, being my exam committee member and sharing your knowledge with me. I would like to acknowledge my classmates in Msc track Geo-Energy Engineering for teaching me and motivating me to step out of my comfort zone.

Finally, I am also thankful to my former employer and tutors who encouraged me to start the journey. A special thanks should be given to my friends, parents, and girlfriend, Jing Zhang, for their support and beliefs in me.

Ziliang Zhang
Delft, August 2022

Contents

List of Figures

List of Tables

1 Introduction

Greenhouse gas emissions from human activities, such as consumption of fossil fuels, pose a threat to the stabilization of atmospheric greenhouse gas concentration. The goal of preventing dangerous anthropogenic interference on climate system and reaching net zero emission are widely accepted to mitigate climate change challenge. Apart from switching to renewable energy sources and reduce energy consumption, capturing and storing CO2 chemically or physically is also proposed as a technology option to reduce net CO2 emissions [20].

Carbon dioxide capture and storage (CCS) has been widely recognized as a straightforward solution to reduce greenhouse gas emissions, because of its promising capacity and technical feasibility. In this approach, the CO2 emissions from large-point source emitters, such as power plants and factories, can be efficiently collected and transported to storage sites. The storage operation normally refers to the process injecting and storing CO2 in a secure geological container, which requires an impermeable unit above as caprock and a porous unit as reservoir to store CO2 successfully [4].

1.1 The candidates of CCS

To meet the prerequisites of geological sequestration, such as capacity, containment and injectivity, there are mainly four types of storage sites under investigation. The characteristics of different geological formations are given below.

- **Depleted oil and gas reservoirs:** Storage in previously producible oil and gas fields are the most tangible solution since the reservoirs are well recognized and adequate infrastructure already exists. In addition, the sealing properties of caprock are proved by storing oil and gas securely over millennia.
- **Saline aquifer formations:** Saline aquifers are good potential targets because of their prevalence in sedimentary basins and enormous storage capacity. It provides an alternative solution in the areas where depleted oil and gas reservoirs are not available. However, this storage option generally requires data acquisition at initial development stage comparing with storage in oil and gas reservoirs.
- **CO2 storage during enhanced coal bed methane recovery:** Methane can be desorbed from coal surface as CO2 flow through large fracture networks in coal beds, during which methane recovery is raised significantly. Depending on the CO2 adsorption capacity, CO2 storage can happen in coal beds that are shallower than other storage site types [27].
- **CO2 storage during enhanced oil recovery:** During the widely applied tertiary recovery process, CO2 can also be injected in mature fields to remove trapped oil in rocks, and CO2 storage becomes the added benefit of the EOR process.

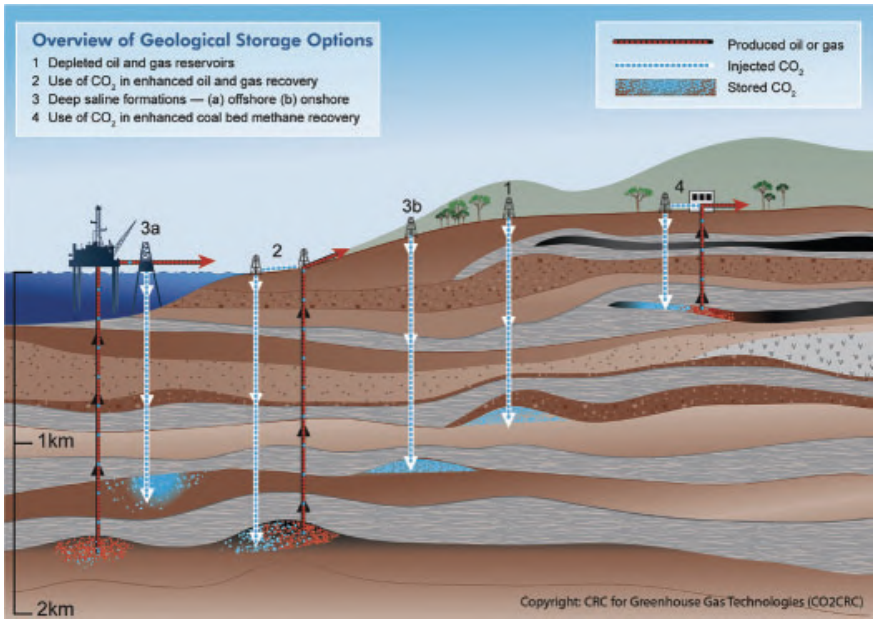

Figure 1.1: Targets of geological CO2 storage.

The different storage options are illustrated in Figure 1.1. This research will mainly focus on CO2 storage in saline aquifers, because of its high storage capacity and availability in the areas near larger emitters.

1.2 Trapping mechanisms

The trapping mechanisms, by which the injected supercritical CO2 is securely trapped in saline aquifers, have been well recognized, including:

- **Structural and stratigraphic trapping:** After CO2 is injected into the reservoirs, CO2 tends to migrate upward because of buoyant forces, and ends up in some topographical features, such as under impermeable caprock and sealed faults. It can also be trapped as a mobile phase in stratigraphic traps, which are formed by changes in rock type.
- **Residual trapping:** also called as capillary trapping. After injection stops, brine tends to reinvade the pore space saturated by CO2, because of the wettability of reservoir rocks to brine. The imbibition process occurs mostly to areas near wellbore and the thin plume that spreads under caprock. As some CO2 is left behind and loses its spatial continuity, those individual droplets of CO2 surrounded by brine would be residually trapped.
- **Solubility trapping:** A small amount of CO2 can dissolve in brine when these two phases are contact with each other during injection and migration. Over time, brine dissolved with CO2 descends to the reservoir bottom in the form of convective fingers because it is heavier than pure brine. The amount of CO2 can be dissolved into

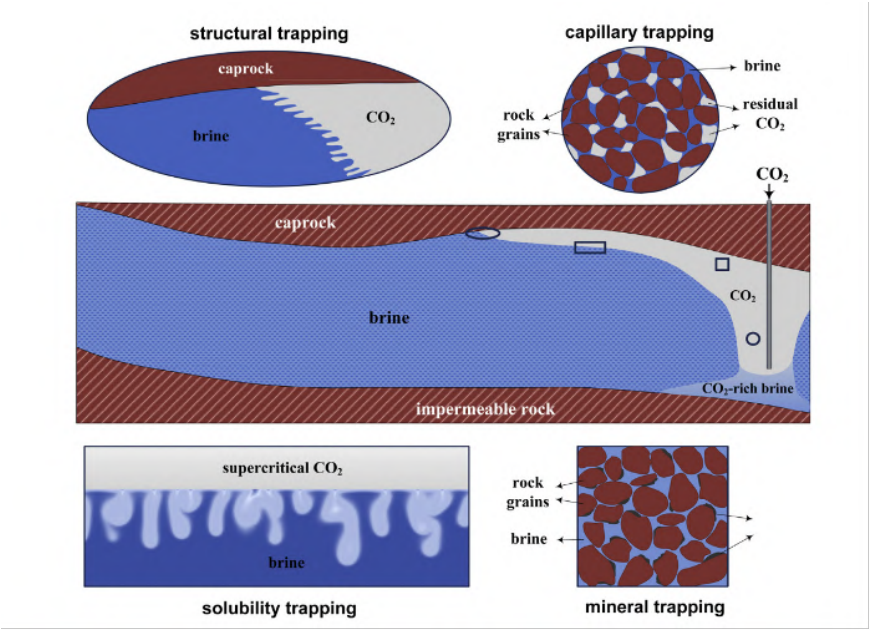

Figure 1.2: Trapping of injected CO2 by different mechanisms [10].

brine relies on pressure, temperature, and salinity of brine, and their effects on CO2 dissolubility have been extensively studied in literature [7] [25].

- **Mineral trapping:** Dissolution of CO2 in brine may be precipitated as carbonate minerals and trapped in this more permanent form. However, this trapping happens on a much larger time scale because of the slow rate of chemical reaction [33].

Although the trapping mechanisms are clearly classified as shown in Figure 1.2, it should be noted that the time scales on which different mechanisms act are not separated and might overlap with each other. Thus, it is necessary to investigate those mechanisms in a unified framework so that the interconnection and their influence on each other can be well understood.

1.3 Reservoir grids

To simulate fluid flow in porous media, the continuous reservoir in the real world needs to be subdivided into finite number of discrete elements. In addition, temporal development also needs to be discretized, so that the properties within an element at any time can be regarded as constant. It is believed that more reliable simulation results can be reached if the reservoir grid can approximate the real reservoir better, which however requires a larger number of cells to represent the complex geometries. Thus, how to discretize a reservoir is always a tradeoff between computation efficiency and numerical accuracy.

The simplest reservoir grid is the cartesian grid, which consists of a set of cube-shaped cells. This type of grid can be uniquely defined, only knowing the size of each cell and the

number of cells at three directions. Although the cartesian grid has the defect that approximating complex geometries poorly, it is the most widely applied reservoir grid because of its numerical stability.

However, cartesian grid sometimes can not offer a good representation of reservoir because of complex geological features, such as faults, erosion and irregular reservoir boundaries (erosion and pinch-out). Meanwhile, corner point grid (CPG) has become the industry-standard approach because it can represent complex reservoir geometries in a more realistic way and improve the accuracy. Corner point gird is a type of structured grid, which has a set of cells that are six-sided with eight nodes. All cells are logically organized in a regular scheme, which means that the position of each cell is uniquely defined by its index. In addition, the nodes at the top and bottom surface of each cell in one column are restricted on a straight line. Since each cell in corner point grid is defined individually with its eight nodes and the restriction on the lines, it is possible to model complex geological features, such as faults or pinch-outs, with degenerate cells. Thus, corner point grid has the advantage of modelling complex geological features more accurately, which plays important roles in fluid flow pattern in field-scale reservoirs [6].

1.4 Research goals

In this study, a simulation method is employed to investigate the complex displacement process between CO2 and brine during a lifelong process of injection and migration. To better understand the dynamic CO2 flow behaviors and the interplay of different trapping mechanisms, one of the research goals is to model different underlying complex physics, such as hysteresis behavior, dissolution, and capillarity, in a unified compositional framework. However, efficient numerical simulation of such complex coupled fluid physics in a large domain is challenging. Thus, a parameterized method for essential trapping physics is proposed to improve computation efficiency.

Another research goal is to extend compositional simulation of CO2 storage to corner-point grid with complex geometries. The existing compositional simulator in DARSim is mainly for the structured cartesian grids, which is challenging to provide an accurate representation of the field-scale reservoir, as subsurface media often include complex geological features, such as faults, erosion, and irregular reservoir boundaries (erosion and pinch-out). On the other hand, corner point grid (CPG) has become the industry-standard approach because it has the flexibility to handle its eight corner points individually and can represent complex reservoir geometries in a more realistic way. Thus, this is a significant step towards applying the proposed compositional framework to industry applications.

1.5 Thesis layout

This work is structured as follows: Firstly, the governing equations describing the compositional flow in the CO2-brine system and Overall-composition formulation are introduced in Chapter 2. Following that, the mathematical description of discretization and solution strategy are briefly explained.

In Chapter 3, different physical models considered in this work and their parameterization results are presented. We then present a basic introduction of corner point grid along

with the different treatment for transmissibility calculation for this type of reservoir gird in Chapter 4.

In Chapter 5, the physics considered in the composition framework are benchmarked by a problem of CO2 injection into layered sand-shale model. After that, the simulation on cartesian gird and corner point gird are compared in terms of quantitative and qualitative results. At the end, simulations on a field-scale reservoir model during a lifelong period are presented to show the impact of various physics, migration path, linear trapping coefficient and aquifer depth.

In Chapter 6, roles of different physics playing in the full cycle of CO2 injection and migration are summarized, and their impact on trapping amount are concluded. In Chapter 7, possible future work based on this research is briefly explained.

2 Governing equations

2.1 Compositional formulation

2.1.1 Mass conservation

To mathematically describe the compositional flow and transport in porous media, mass conservation law states:

$$\frac{\partial}{\partial t}\left(\phi \sum_{\alpha=1}^{n_{ph}} x_{c,\alpha}\rho_\alpha S_\alpha\right) + \nabla \bullet \left(\sum_{\alpha=1}^{n_{ph}} x_{c,\alpha}\rho_\alpha u_\alpha\right) - \sum_{\alpha=1}^{n_{ph}} x_{c,\alpha}\rho_\alpha q_\alpha = 0, \;\; \forall c \in 1, \; \ldots, \; n_c \tag{2.1}$$

In Equation 2.1, α is the fluid phases and can be liquid or vapor in our case. ρ_α and S_α in the accumulation term are the molar density and saturation of phase α, while q_α in source term is the flow rate of same phase. Most importantly, $x_{c,\alpha}$ in all the three terms is the molar fraction of components in phase α, and it distinguishes compositional flow from two-phase flow because components are allowed to be split into different phases. u_α in convective term is the phase velocity and Darcy's law describes the flow of fluid phases as:

$$u_\alpha = \frac{k k_{r,\alpha}}{\mu_\alpha} \nabla \left(p_\alpha - \widetilde{\rho}_\alpha g h\right), \;\; \alpha = 1, \; \ldots, \; n_{ph} \tag{2.2}$$

in which k is the rock permeability, and $k_{r\alpha}$, μ_α and $\widetilde{\rho}_\alpha$ are phase relative permeability, phase viscosity and phase mass density respectively. The pressure difference between different phases is described by capillary pressure function in Equation 2.3:

$$p_\alpha - p_\beta = p_{c_{\alpha,\beta}}, \;\; \forall \alpha \neq \beta \in 1, \; .., n_{ph} \tag{2.3}$$

In addition, the saturation constraint reads:

$$\sum_{\alpha=1}^{n_{ph}} S_\alpha = 1 \tag{2.4}$$

2.1.2 Thermodynamic equilibrium

When multiple phases present, it is usually assumed all phases reach thermodynamic equilibrium [5], which can be described as:

$$f_{c,\alpha}\left(p, \; x_{c,\alpha}\right) - f_{c,\beta}\left(p, \; x_{c,\beta}\right) = 0, \;\; \forall \alpha \neq \beta \in \left\{1, \; .., n_{ph}\right\} \tag{2.5}$$

The phase constraint based on molar fraction term reads:

$$\sum_{c=1}^{n_c} x_{c,\alpha} = 1, \;\; \alpha = 1, \; \ldots, \; n_{ph} \tag{2.6}$$

The overall mole friction of component c, z_c, can be defined as:

$$z_c - \sum_{\alpha=1}^{n_{ph}} \nu_\alpha x_{c,\alpha} = 0, \quad \forall c \in 1, \ .., n_c \tag{2.7}$$

In which ν_α is the mole friction of phase α, and it can be expressed as a function of saturation:

$$\nu_\alpha = \frac{S_\alpha \rho_\alpha}{\sum_{\alpha=1}^{n_{ph}} S_\alpha \rho_\alpha} \tag{2.8}$$

2.2 Overall-composition formulation

To solve the isothermal compositional problem, different formulations that use different variable set have been studied in literature [32]. Overall composition variable set sometimes is preferred because no variable substitution is needed. In other words, equation and variables are the same for every cell comparing with natural variable set, although phase equilibrium computation cannot be avoided for every grid cell.

In our two-component and two-phase system, overall composition variable set is chosen, and primary variables include one phase pressure and one overall molar fraction. With the defined overall molar composition, the mass conservation equation for each component states,

$$\frac{\partial}{\partial t}\left(\phi \rho_T z_c\right) + \nabla \bullet \left(\sum_{\alpha=1}^{n_{ph}} x_{c,\alpha} \rho_\alpha u_\alpha\right) - \sum_{\alpha=1}^{n_{ph}} x_{c,\alpha} \rho_\alpha q_\alpha = 0, \quad \forall c \in CO2, \ brine \tag{2.9}$$

In which ρ_T is total density, and it can be expressed with phase density and saturation as:

$$\rho_T = \sum_{\alpha=1}^{n_{ph}} S_\alpha \rho_\alpha \tag{2.10}$$

2.3 Discretization

The nonlinear system of equations is solved using finite volume discretization in space and implicit time discretization scheme, in which all properties are evaluated on next time step. The discretized equation for component c in cell i in residual form is given by:

$$r_{c,i} = \frac{V}{\Delta t}\left(\left(\phi \rho_T z_c\right)^{n+1} - \left(\phi \rho_T z_c\right)^n\right) + \sum_{j=1}^{n_b} T_{c,ij}\left(p_i - p_j\right) + T_{c,ij}\widetilde{\rho}_\alpha g\left(h_i - h_j\right) + T_{c,i}^w\left(p_i - p_w\right) \tag{2.11}$$

In which $T_{c,ij}$ is the transmissibility between grid cell i and one of its neighboring cells j:

$$T_{c,ij} = \frac{k_{ij}^H A_{ij}}{d_{ij}}\left(x_{c,g}\rho_g \frac{k_{rg}}{\mu_g} + x_{c,l}\rho_l \frac{k_{rl}}{\mu_l}\right)_{ij} \tag{2.12}$$

It can be used to formulate the flux between these two cells with pressure difference as shown in Equation 2.11. Similarly, the connectivity between the well and the cells where it perforates, $T^w_{c,i}$, can be expressed with well index WI as:

$$T^w_{c,i} = \ WIk_i(x_{c,g}\rho_g\frac{k_{rg}}{\mu_g} + x_{c,l}\rho_l\frac{k_{rl}}{\mu_l})^w \tag{2.13}$$

2.4 Solution strategy

The residual equations of the two components are nonlinearly dependent on the primary variables (p_l and z_{CO2}). Newton-Raphson method is used to linearize the system of nonlinear equations as:

$$r^{\nu+1}_{c,i} \approx r^{\nu}_{c,\{i\}} + \frac{\partial r^{\nu}_{c,\{i\}}}{\partial p_l}|^{\nu}\delta p^{\nu+1}_l + \frac{\partial r^{\nu}_{c,\{i\}}}{\partial z_{CO2}}|^{\nu}\delta z^{\nu+1}_{CO2} = 0 \tag{2.14}$$

In which ν and $\nu+1$ are the current and next iteration step respectively. Then the linearized equations can be solved iteratively:

$$J^v\delta x^{v+1} = -r^v \tag{2.15}$$

In which J^v and r^v are Jacobian and Residual matrix, while δx^{v+1} is the primary variable update. The same function in matrix multiplication form is given as below:

$$\begin{pmatrix} \frac{\partial r_{CO2}}{\partial p_l} & \frac{\partial r_{CO2}}{\partial z_{CO2}} \\ \\ \frac{\partial r_b}{\partial p_l} & \frac{\partial r_b}{\partial z_{CO2}} \end{pmatrix} \begin{pmatrix} \delta p_l \\ \\ \delta z_{CO2} \end{pmatrix} = - \begin{pmatrix} r_{CO2} \\ \\ r_b \end{pmatrix} \tag{2.16}$$

The process is repeated until it reaches non-linear convergence, which mathematically means the infinite norm of the residual and variable update are less than a certain tolerance. In addition, an adaptive time stepping strategy is employed to reduce the number of iterations needed to reach convergence. In this work, the time step size is dynamically changed between user defined maximum and minimum time step size, based on the number of iterations needed to converge.

3 Physical models

Behind the general trapping mechanisms listed in Chapter 1, various physical effects are happening in pore spaces during CO2 sequestration. In this work, three essential physics, including dissolution, capillarity and hysteresis, are considered in a unified compositional framework. The implementation and the proposed parameterized spaces for different trapping physics are given in this chapter.

3.1 Dissolution

The solubility of CO2 in brine depends on several physical parameters, including pressure, temperature and water salinity [25]. In this work, at given temperature and salinity, the volume of CO2 that can be dissolved into unit volume of brine, R_s or the solution CO2-brine ratio gives the amount of CO2 dissolved into brine at different pressure.

3.1.1 Stability test

However, the amount of CO2 present in brine for each reservoir grid also depends on available CO2 in that cell [12]. Thus, a stability test is preformed to check the number of phases existing in each cell after the primary variables are updated at each iteration. There is only liquid phase existing in the cell if the following rule is satisfied:

$$\sum_{c=1}^{n_c} z_c k_c < 1 \tag{3.1}$$

In which k_c is the k values of component c, which is the ratio between mole frictions in gas and liquid phase:

$$k_c = \frac{x_{c,g}}{x_{c,l}} \tag{3.2}$$

k value is a function of pressure and temperature and it governs how one component is split into phases. In this isothermal system, assuming brine only present in liquid phase, the k values for CO2 and brine are given by:

$$k_{CO2} = \frac{\rho_{CO2}^{STC} R_s + \rho_b^{STC}}{\rho_{CO2}^{STC} R_s}, \quad k_b = 0 \tag{3.3}$$

3.1.2 Two-phase state cells

In two-phase state cells, CO2 exists in both liquid and gas phase. To determine the amount of CO2 in liquid phase, CO2 solubility at given temperature and salinity is predicted by a thermodynamic model that equates chemical potential [25] [13]. The solution CO2-brine ratios can be predicted by using the mole fraction of CO2 in liquid phase obtained from the CO2 molality in brine as:

$$R_s = \frac{\rho_b^{STC} x_{CO2,l}}{\rho_{CO2}^{STC}(1 - x_{CO2,l})} \tag{3.4}$$

In which STC is standard condition. In our isothermal system, assuming the salinity of brine is constant, the solubility of CO2 is only function of pressure. Thus, a direct relationship between Rs and pressure can be generated and stored in a lookup table during an offline stage before simulation starts. The R_s value can be directly read from the table with known pressure, as shown in Figure 3.1.

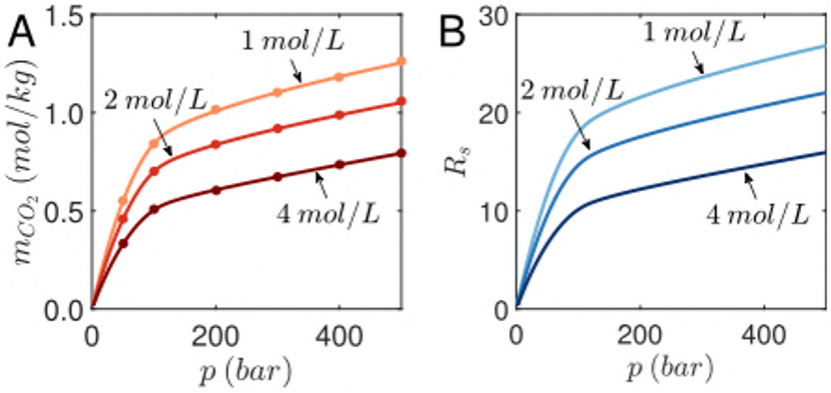

Figure 3.1: The predication of CO2 solubility in brine at 60°C [24] [33].

3.1.3 Single-phase state cells

For a single-phase cell, the amount of CO2 that can be dissolved in brine is not enough to reach dissolution limit. Thus, if only liquid exits in a cell, the solution CO2-brine ratio is computed based on the overall molar fraction of CO2 as:

$$R_s = \frac{\rho_b^{STC} z_{CO2}}{\rho_{CO2}^{STC}(1 - z_{CO2})} \tag{3.5}$$

3.2 Capillarity

Capillary pressure is defined as pressure difference across the curved interface between non-wetting and wetting phases. Mathematically, capillary pressure can be expressed as:

$$P_c = \frac{2\sigma \cos(\theta)}{r} \tag{3.6}$$

In which σ is the interfacial tension between the two fluids, and θ is the contact angle between rock and fluid, and r is the pore radius. As indicated by Equation 3.6, capillary pressure depends on fluid, rock-fluid interaction parameters and rock property. For example, capillary pressure in low permeability rock with smaller pore radius is larger than rock with high permeability rock containing the same fluids [11].

CO2 can be collected under or even outside structural and stratigraphic traps at high saturation, when the buoyancy force cannot overcome the capillary forces caused by narrower pore throat of caprock, such that CO2 cannot enter the overlying pore space [14]. In addition, a portion of non-wetting phase is left as discontinuous ganglia and becomes immobilized because of capillary forces, which depend on pore structure, wettability and fluid and flow properties, during non-wetting phase displacement by wetting-phase. The residual saturation of non-wetting phase is nonzero even if capillary pressure approaches zero.

3.3 Hysteresis

The constitutive relationship, such as relative permeability and capillary pressure, are not only functions of saturation [17], but also depend on the history of saturation, i.e., the drainage or imbibition process. As given by Figure 3.2, the hysteretic effect in relative permeability experiment data of strongly water-wet Berea sandstone is represented by the difference between drainage and imbibition curves. Another example of the hysteresis behavior can be observed in capillary pressure curves modelled by the Leverett J-function, as given by Figure 3.3.

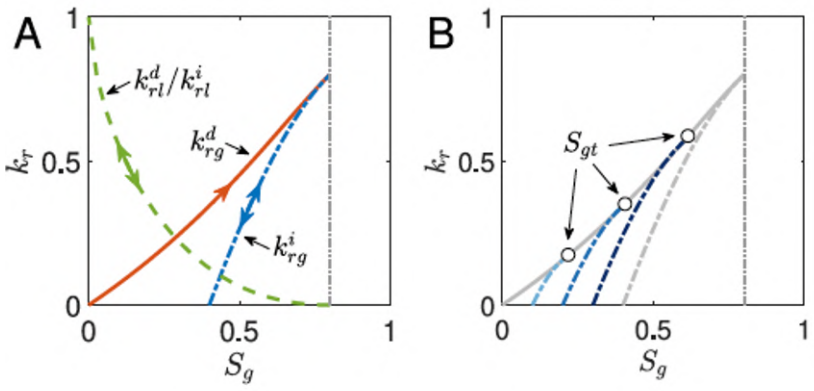

Figure 3.2: Illustration of hysteretic model of relative permeability curves. (A) Primary drainage and imbibition curves for liquid and gas phases. (B) Hysteresis behavior modelled by the scanning curves that generated at the turning points at S_{gt}=0.2, 0.4, and 0.6 [21] [33].

When it comes to CO2 storage field operation, the hysteresis effect mainly refers to the behavior that different relative permeability or capillary pressure curves are followed during drainage and imbibition process. Mainly drainage process is happening in the pore space during CO2 injection. During this process, CO2 saturation keeps increasing following the

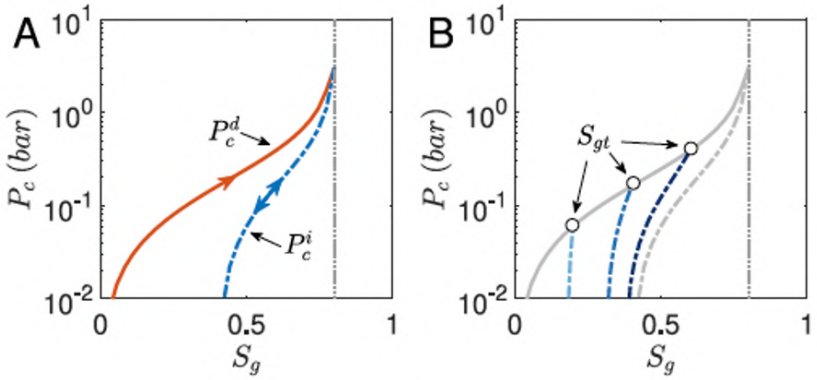

Figure 3.3: Illustration of hysteretic model of capillarity pressure curves (A) Primary drainage and imbibition curves. (B) Hysteresis behavior modelled by the scanning curves that generated at the turning points at S_{gt}=0.2, 0.4, and 0.6 [33].

primary drainage curve, while brine saturation decreases until its residual saturation. After injection stops, the process turns to imbibition and its relative permeability changes along the primary imbibition curve.

3.3.1 Scanning curve

However, the transition from drainage to imbibition process does not always happen at the maximum gas saturation. The drainage process is often interrupted before S_{CO2} reaches its maximum, and changes to imbibition process. To ensure the transition is continuous, a series of scanning curves based on primary bounding curves are constructed as shown in Figure 3.4 [18]. The point where transition happens is called as turning point, S_{gt}, and the gas relative permeability decreases to 0 when gas saturation reaches residual saturation. It needs to be noted that both drainage and imbibition can happen along scanning curve. In other words, no new scanning curve would be generated on old scanning curves for alternation of flow process to maintain simulation stability.

3.3.2 Scanning curve surface

In the previous simulation work [33], the scanning curve for each cell is constructed after the flow process is determined cell by cell. The determination of the process is based on comparing gas saturation from the previous two time steps, or n and n-1. For example, if $S_g^n < S_g^{n-1}$ on primary drainage curve, it indicates the process is already transitioned to the scanning curve corresponding to $S_g^{n-1}(S_{gt})$.

The disadvantage of this workflow is scanning curves are constructed repetitively. Moreover, its negative impact on computation efficiency is more obvious for larger amount of grid cells. For example, the scanning curve needs to be constructed again even though different cells share a same turning point. Another example is when a cell stays on the same scanning

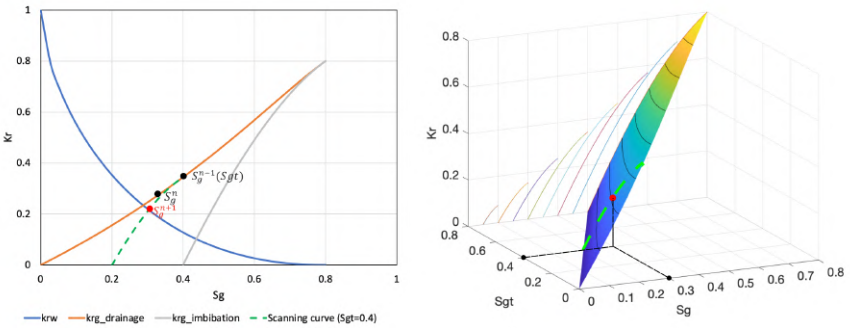

Figure 3.4: Illustration of hysteretic relative permeability models. (A) Determination process based on scanning curves. (B) Determination process based on the proposed scanning curve surface.

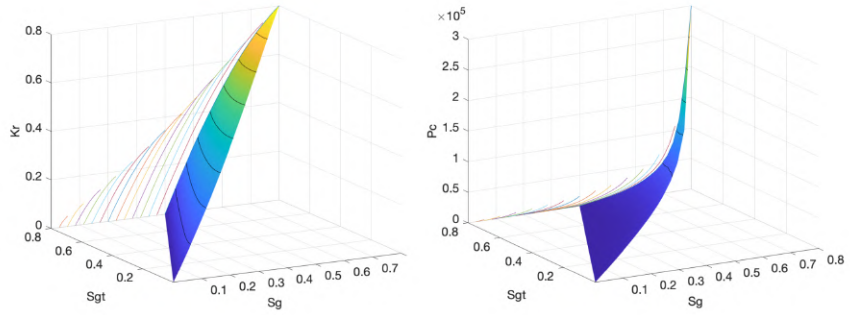

Figure 3.5: Scanning curve surfaces to model the hysteretic behaviors of relative permeability and capillary pressure.

curves for several time steps, the scanning curve needs to be constructed for every time step since the information is not stored.

Here we propose a new workflow, in which a scanning curve surface for the constitutive relations can be generated at an offline stage as given by the right plot of Figure 3.4 and Figure 3.5. After the process for each cell is determined, the gas relative permeability or capillary pressure can be read directly from the surface, knowing the pair of gas saturation and turning point. In this way, we avoid constructing the scanning curves repetitively, and improve simulation efficiency.

4 Corner point grid

4.1 Components

A structured grid has a set of six-sided cells with eight nodes, which are also logically organized with its (I, J, K) index. Instead of being defined arbitrarily, the eight corner nodes of corner point grid are restricted on a set of straight non-horizontal lines, which are referred to as coordinate lines. Those coordinate lines are defined by coordinates $(x,\ y,\ z)_{Top}$ and $(x,\ y,\ z)_{Btm}$. Uniquely defined by (I, J) index, the set of coordinate lines forms the skeleton of corner point grid.

Each cell in corner point grid is defined by four neighboring coordinate lines and eight corner depth. In other words, exactly two corner nodes are located on one coordinate line for top and bottom faces respectively. The cell has a topological cube shape when all the eight nodes are different. However, the two nodes on one or up to four coordinated lines of that cell can coincide. In this case, the cell is a degenerate cell, which has one or more edges thickness that equal to zero. Degenerate cells provide the flexibility to model cells that do not have a normal appearance, such as wedge cells in a pinch-out zone or zero-thickness cell, because the number of layers can remain the same and the logical index scheme of corner point gird is maintained.

4.2 Corner point gird in Eclipse

In Eclipse, the two important components of corner point grid, including coordinate lines and corner depths, are defined by keywords *COORD* and *ZCORN* respectively. Uniquely defined by (I, J) index, each coordinate line is formed by two coordinates. For example, if the corner point grid has N_x and N_y of cell in x and y directions, the number of coordinate lines in the two directions would be $N_x + 1$ and $N_y + 1$. All coordinate lines are stored in book page format, in which I runs from 1 to $N_x + 1$ for each J between 1 and $N_y + 1$. The intersection between coordinate lines and corner depths defined by *ZCORN*, can uniquely determine the coordinates of each grid cell. *ZCRON* is also input in book page format, with I running from 1 to N_x firstly, and then J from 1 to N_y and K from 1 to N_z.

4.3 Corner point grid geometry

The tetrahedral subdivision method implemented in MRST simulator [19] is employed to acquire a variety of cell geometry information, including face centroids, face areas, face normal, cell centroids and cell volumes, based on the known points forming a face: $\vec{p}(\alpha_1), ..., \vec{p}(\alpha_m)$.

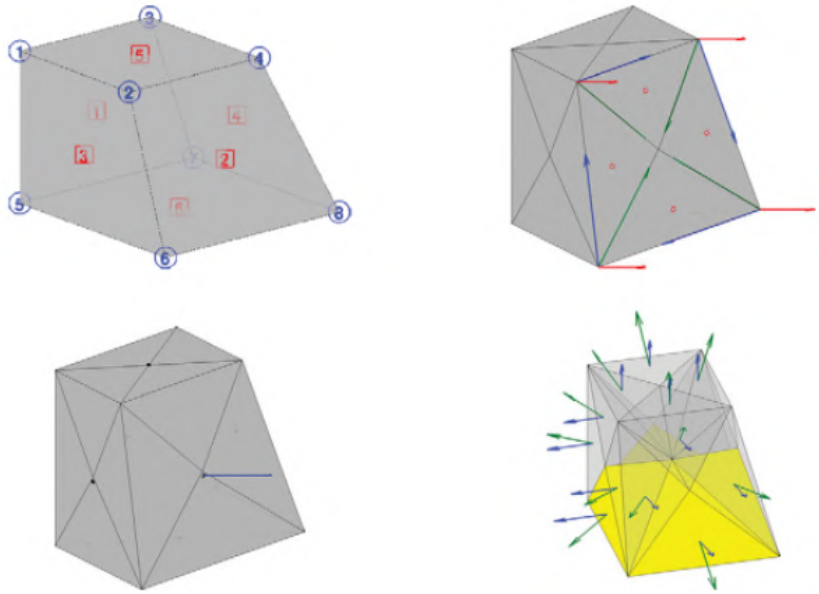

Figure 4.1: Computation of geometry information of a corner point grid cell in MRST.

In MRST, hinge point, defined as the center point of the m points forming a face, can be obtained as:

$$\vec{p}_h = \frac{\sum_{k=1}^{m} \vec{p}(\alpha_k)}{m} \tag{4.1}$$

Then, the surface is tessellated into m triangles, which are specified by $\vec{p}(\alpha_k)$, $\vec{p}(\alpha_{k+1})$ and $\vec{p}_h$. Based on the three vertexes, the normal vector $\vec{n}^k$, area A^k and center point $\vec{p}_c^k$ corresponding to each of the triangles can be obtained. Furthermore, the area A_f, centroid $\vec{c}_f$ and normal vector $\vec{n}_f$ related to the face are computed using the geometry information of triangles. To obtain the geometry of cells, the center points of cells, defined as the average of the face centroids, are computed as:

$$\vec{c}_c = \frac{\sum_{f=1}^{m_f} \vec{c}_f}{m_f} \tag{4.2}$$

Then, tetrahedral subdivision, in which the center point is connected to the m_t face triangles, is conducted as given by the lower right plot in Figure 4.1. The vector, defined as $\vec{c}_r^k = \vec{p}_c^k - \vec{c}_c$, and volume V^k related to each tetrahedral are computed. Finally, the cell volume V, and centroid $\vec{c}$ are acquired based on the geometry information of tetrahedral.

4.4 Two-Point Flux Approximation

To illustrate the finite volume discretization of different types of grids, the convective term in incompressible single-phase system can be used as an example for simplicity, because

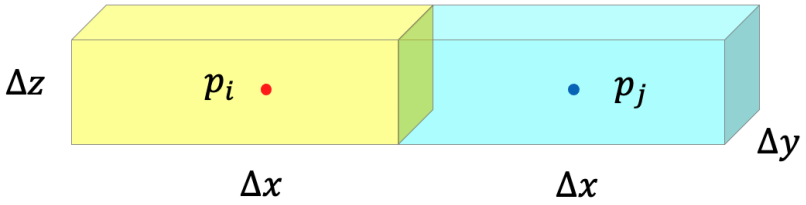

Figure 4.2: Computation of the flux between two neighboring cartesian grid cells.

only convective term in mass conservation equation is realted to neighboring cells [15].

$$\nabla \bullet (\vec{u}) = q \tag{4.3}$$

The finite volume method with two-point flux approximation is usually used to discretize the convective term. Considering a single cell Ω_i in the discrete grid as control volume, the integral over volume equal to the flux across the closed surface according to Divergence theorem:

$$\int_{\Omega_i} \nabla \bullet (\vec{u})\, dV = \int_{\partial\Omega_i} \vec{u} \bullet \vec{n}\, dS \tag{4.4}$$

Thus, the next step is to use Darcy's law to compute the flux across each face of the cell. For cartesian grids in Figure 4.2, the flux can simply be derived based on Darcy's law,

$$u_{ij} = \frac{k_{ij}^H A_{ij}}{d_{ij}} \left(p_i - p_j\right) = T_{ij}(p_i - p_j) \tag{4.5}$$

In which T_{ij} is usually referred to as transmissibility term, and it indicates the connectivity between the two cells.

For corner point grid, the derivation of flux between two cells is more complicated because the distance between every two cells is not known as shown in Figure 4.3. The flux between two neighboring grid cells i and j is given by:

$$u_{i,\,j} = \int_{\Gamma_{i,\,j}} \vec{u} \bullet \vec{n}\, dS \tag{4.6}$$

In which $\Gamma_{i,\,j}$ is the half interface between cell i and j that associated with control volume Ω_i. It has a twin half interface $\Gamma_{j,\,i}$ that has identical area and opposite normal vector. At this step, the pressure at the face centroid, $\pi_{i,\,j}$, is newly introduced to express one-sided pressure difference. Assuming the reconstructed pressure at cell center equals to average pressure within the cell, p_i, the one-sided finite difference between the pressure at the face centroid and the pressure at some point inside the cell reads:

$$u_{i,\,j} \approx A_{i,\,j} K_i \frac{\left(p_i - \pi_{i,\,j}\right) \vec{c}_{i,\,j}}{\left|\vec{c}_{i,\,j}\right|^2} \vec{n}_{i,\,j} \tag{4.7}$$

where $\vec{c}_{i,\,j}$ is the vector from cell centroid to face centroid, and it is not necessarily parallel to the face normal vector, $\vec{n}_{i,\,j}$. Together with face area, $T_{i,\,j}$ the one-sided transmissibilities

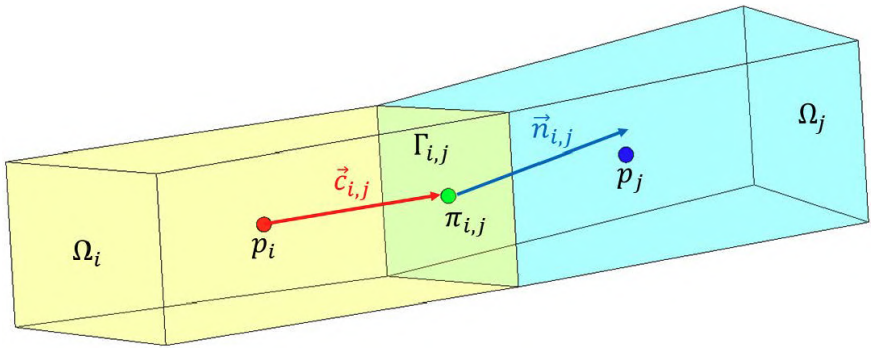

Figure 4.3: Computation of the flux between two neighboring corner point grid cells.

or half transmissibilities that associated with cell i is given by:

$$T_{i,\,j} = A_{i,\,j} K_i \frac{\vec{c}_{i,\,j} \bullet \vec{n}_{i,\,j}}{\left|\vec{c}_{i,\,j}\right|^2} \tag{4.8}$$

It gives a two-point relation between the flux across a cell face and the the pressure difference between the cell and face centroids.

$$u_{i,\,j} = T_{i,\,j}(p_i - \pi_{i,\,j}) \tag{4.9}$$

Thus, it is possible to express the one-sided pressure difference between the two cells as:

$$T_{i,\,j}{}^{-1} u_{i,\,j} = (p_i - \pi_{i,\,j}) \tag{4.10}$$

Imposing continuity of fluxes and face pressure, it would lead to:

$$u_{i,\,j} = -u_{j,\,i} = u_{ij}, \quad \pi_{i,\,j} = \pi_{j,\,i} = \pi_{ij} \tag{4.11}$$

Then the introduced interface pressure is eliminated by combining the two equations above:

$$u_{ij} = \left(T_{i,\,j}{}^{-1} + T_{j,\,i}{}^{-1}\right)^{-1} (p_i - p_j) \tag{4.12}$$

And the transmissibility, T_{ij}, that associated with the connection between two cells, is derived from half transmissibilities:

$$T_{ij} = \left(T_{i,\,j}{}^{-1} + T_{j,\,i}{}^{-1}\right)^{-1} \tag{4.13}$$

Thus, the derivation of flux across each face for corner point grid provides more generality because the vector from cell to face centroid is not necessarily parallel to normal vector. The transmissibility for cartesian grid can be calculated in the same manner and end up in the same form that is derived from Darcy's law. After transmissibility is calculated, the TPFA scheme approximates the flux across each interface between two cells with two cell average pressure as:

$$u_{ij} = T_{ij}(p_i - p_j) \tag{4.14}$$

5 Simulation results

In this chapter, the results of a series of numerical simulations of CO2 injection and migration in 2D and 3D test cases are presented. They demonstrate the capability of the developed compositional framework modelling the essential physics, such as dissolution, capillarity, and hysteresis. In addition, the simulations on cartesian and corner point grids are compared to show the reliability of the extension work to corner point grid. At the end, a full-cycle CO2 injection and migration in a realistic reservoir model is simulated and the roles of different physics are investigated. The geometry information of synthetic and realistic corner point grid is generated based on the open-source simulator MRST, which can process the ECLIPSE format input file.

5.1 Layered sand-shale model

The first test case is a benchmark study on CO2 injection into a layered sand-shale aquifer, as shown in Figure 5.1. Based on the Sleipner Vest CO2 injection project, the 2D test problem is designed to investigate the key physical processes occurring to CO2 injection in layered formation, such as the viscous to buoyancy-driven flow and CO2 accumulation under capillarity barrier [22] [23] [1]. With this benchmark study, the physical effects, including dissolution and capillarity, incorporated into our compositional framework are validated.

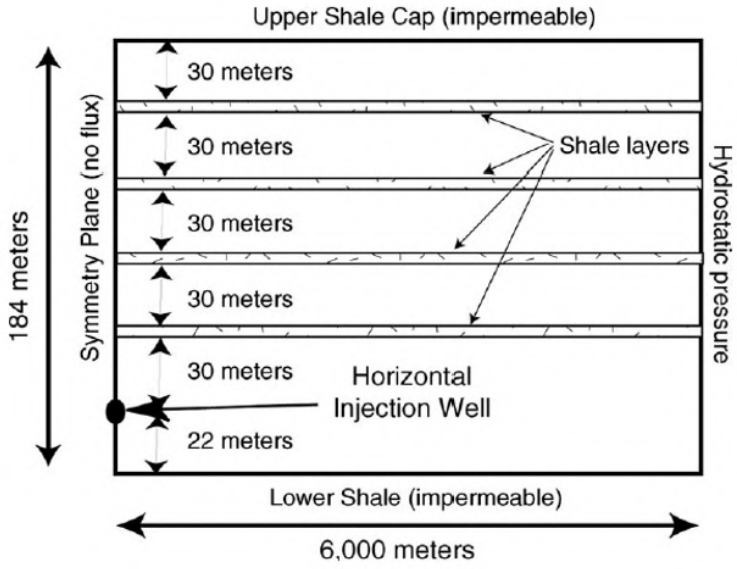

Figure 5.1: CO2 injection into an idealized layered sand-shale formation.

Properties	Symbols	Units	Sand	Shale
Porosity	ϕ	-	0.35	0.1025
Permeability	k	mD	3000	10
Residual gas saturation	S_{rg}	-	0.05	0.05
Residual water saturation	S_{rw}	-	0.20	0.20
Capillary entry pressure	p_{ce}	kPa	3.58	62.00

Table 5.1: Petrophysical parameters of sand and shale layers.

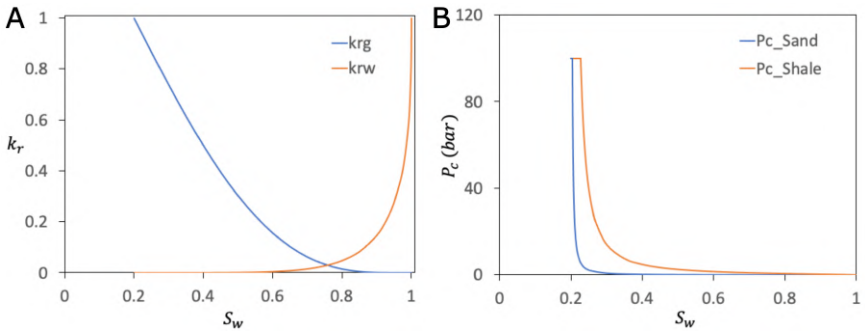

Figure 5.2: Relative permeability and capillary pressure models for sand and shale layers. (A) Relative permeability for both sand and shale layers. (B) Capillary pressure.

The 2D domain is a vertical plane with a length of 6000 meters and height of 184 meters, and only 1-m-thick cross section perpendicular to the horizontal well is modelled. The geometry of the formation is idealized to consist of 5 sand layers that interbedded with 4 low permeability shale layers. The injection well is 30 meters below the lowest shale layer and there is another 22-m-thick sand unit below the well. The reservoir properties for the sand and shale layers are summarized in Table 5.1. The relative permeability and capillary pressure curve for both sand and shale layers are given by Figure 5.2.

The initial formation temperature is $37°C$ and an isothermal condition is assumed. Fluid flow is only allowed at the right boundary, while no heat or mass flux is allowed to across the other three boundaries. The right boundary is fixed at hydrostatic pressure to allow fluid to flow in or out and to avoid over pressurizing the system. The initial pressure at the height where injection well is perforated is about 110 bars.

The gas and water saturation as functions of space and time are obtained to benchmark against results in literature. Figure 5.3 shows the distribution of gas saturation after 2 years of injection. As CO2 is injected into the aquifer, it tends to flow upward when migrating in sand layers because CO2 is less dense than the brine. When injected CO2 reaches the shale layers, CO2 is accumulated below those capillary barriers and a gas column is formed, because a higher capillary entry pressure needs to be exceeded before CO2 can break through. Because CO2 cannot migrate upward freely, CO2 plumes in sand layers below tend to spread and migrate into the aquifer further. The comparison between our simulation results and former research shows good agreement on the distance and the height CO2 plume migrates.

Figure 5.4 shows the CO2 saturation profile at 500 meters from injection well after 2 years.

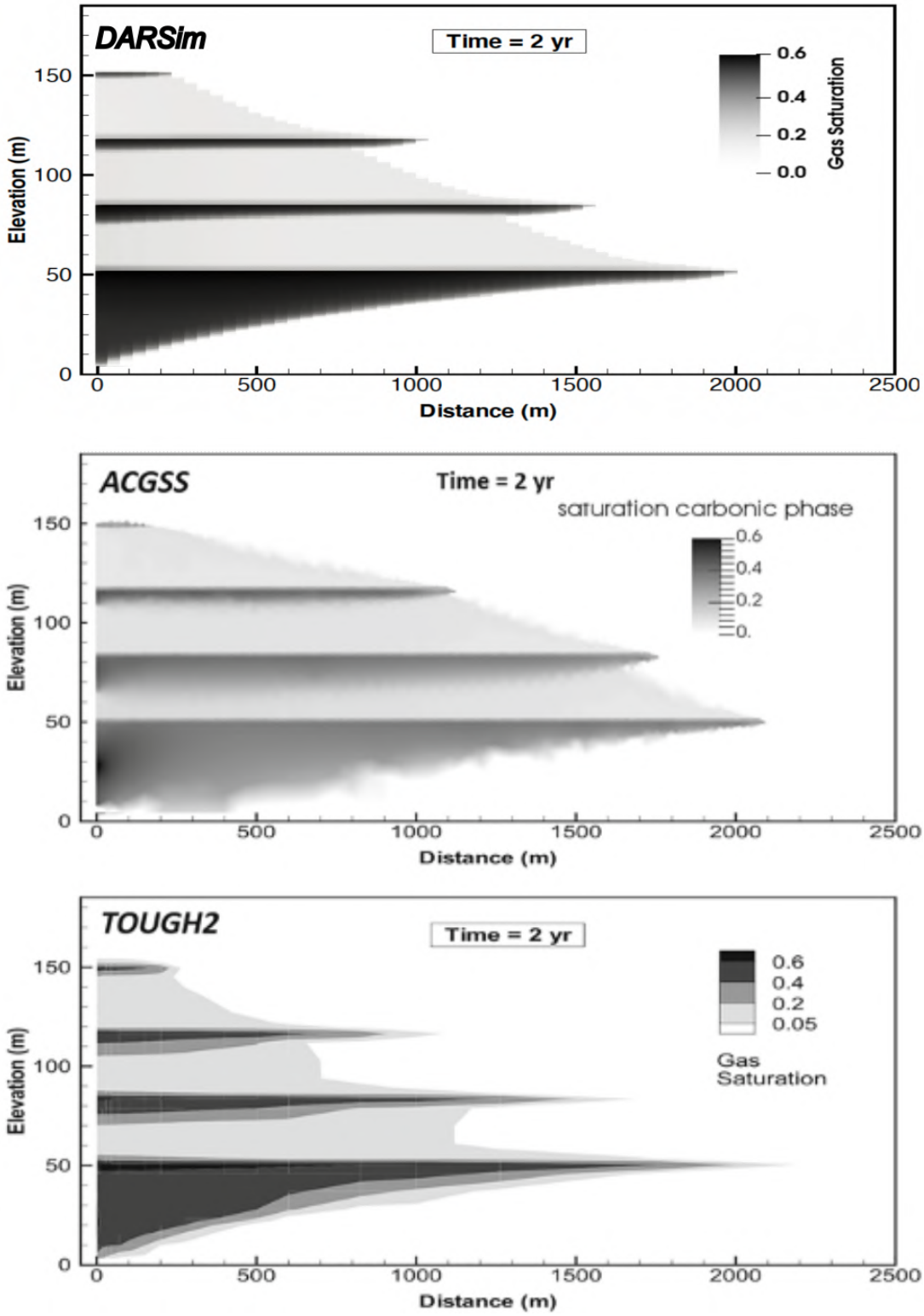

Figure 5.3: Predicted gas saturation profile after 2 year by DARSim (top), ACGSS (middle) and TOUGH2 (bottom).

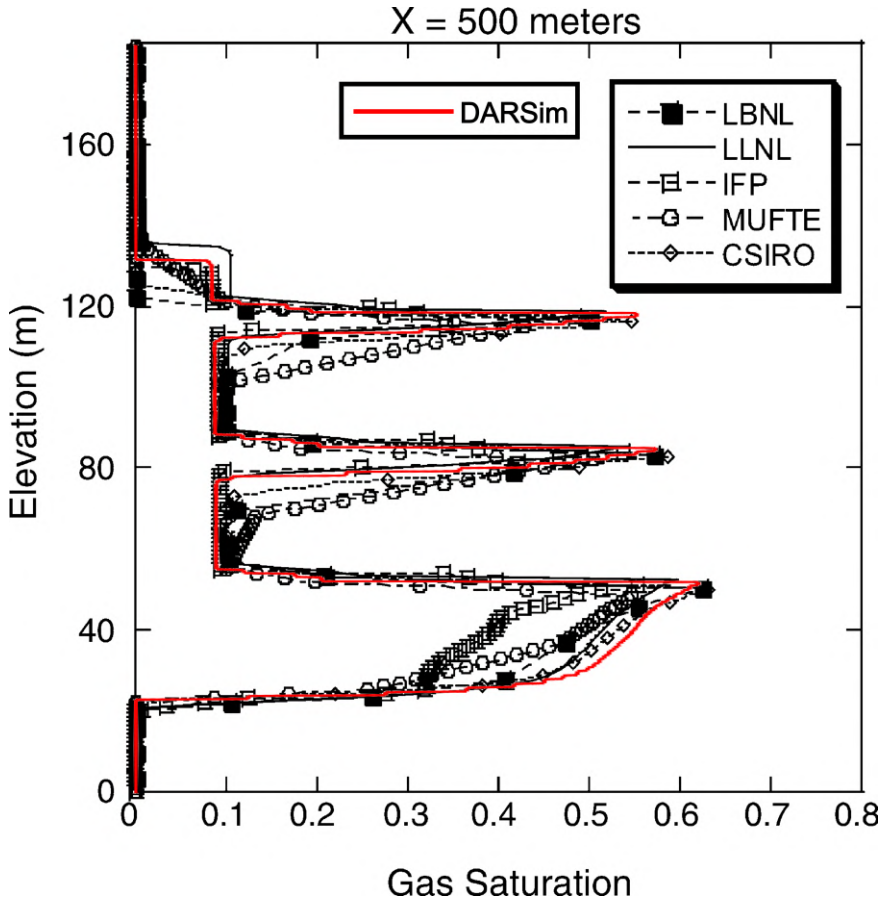

Figure 5.4: Predicted gas saturation profile along a vertical line at 500 m distance from the injection well by DARSim (red) and other benchmark groups (black).

The DARSim simulation result agrees well with results of the benchmark study in literature. High gas saturation intervals in the profile plot represent the CO2 plume under each shale layer. in addition, CO2 saturation gradually increases along the elevation within a CO2 plume. However, there is an abrupt decrease of CO2 saturation to around 0.1 at the interfaces of sand and shale layers. CO2 at the bottom of sand layers has a similar saturation as in shale layers. The highest CO2 plume in Figure 5.3 is missing in the profile plot of the vertical line because the plume did not migrate to 500 meters after 2 years.

5.2 2D Cartesian VS CPG

This test case is designed to evaluate the reliability of the extension of compositional framework to corner point gird. Firstly, the geometry information of a 2D cartesian box is computed and stored as corner point grid, knowing the grid resolution and dimension. Then the simulation results on cartesian grid and converted corner point grid are compared to validate the extension work.

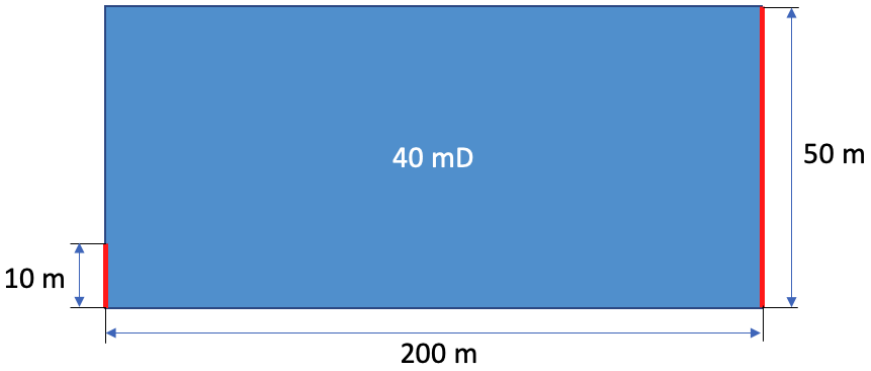

Figure 5.5: Setup of the 2D cartesian box model.

Properties	Symbols	Values	Units
Reservoir length	L	100	m
Reservoir height	H	50	m
Porosity	ϕ	0.2	-
Permeability	k	40	mD
Initial reservoir pressure	p_0	2.5e7	Pa
Bottom hole pressure	p_w	2.5e7	Pa
Reservoir temperature	T	338.15	K
CO2 density at STC	$\rho_{CO_2}^{STC}$	1.98	kg/m^3
Brine density at STC	ρ_b^{STC}	1060	kg/m^3
Brine salinity	$-$	1.0e5	ppm
Injection rate	q	8.0e-5	PV/day
Injection time	t_{inj}	600	day
Simulation time	t_{tot}	36000	day

Table 5.2: Physical parameters and simulation settings of the 2D cartesian box test case.

The aquifer is modelled by a two-dimensional vertical cross section as in Figure 5.5, which has a length of 200 meters and height of 50 meters. The aquifer is discretized by 200 x 50 cells to have a grid resolution of 1 meter by 1 meter. An injection well is placed at the bottom 10 meters of left boundary, and the whole 50 meters at the right boundary is perforated for a production well to allow fluids to flow. CO2 is injected into the aquifer at a rate of 8×10^{-5} pore volume per day for 600 days, and total time of 36000 days are simulated. The depth of the aquifer is set to be deeper than 2500 meters to represent the typical CO2 sequestration targets. Several physical parameters used in the simulation, such as initial pressure and temperature, are summarized in Table 5.2 [16] [33]. The relative permeability and capillary pressure curves presented in Chapter 3 are used during simulation. At the end of simulation, the evolution of CO2 plume at different times and quantitative trapping amount by different storage mechanisms are obtained.

In this work, the simulation results focus on demonstrating the dynamic interaction between CO2 and brine in a lifelong process, including injection and migration periods. The amount

of CO2 trapped by dissolution and residual storage mechanisms are recorded to evaluate the trapping performance quantitatively. The dissolution and residual trapping are quantified by the solution CO-brine ratio and saturation map respectively. An overall trapping amount is determined because it is normally regarded as securely trapped part in hydrodynamic trapping, which is the collective term for structural, dissolution and residual trapping. All those trapping amounts are expressed in scaled total injected amount of CO2 in the reservoir, or the fraction of injected CO2.

In the discussion below, a nondimensionalized elapsed time, t_N, defined as the ratio between the real elapsed time and the duration of injection period, is used because the focus is on how the distribution and trapping amount dynamically change through time, instead of the exact prediction at a specific time step. This treatment indicates that injection period starts from 0 and ends at 1, after which the CO2 injection ceases. In the present results, the distribution of S_g and R_s are visualized at different moments during injection and post-injection periods to provide an insight into the dynamics of interaction between CO2 and brine in the full-cycle process.

The gas saturation at several nondimensional time steps for cartesian grid are given by the left plot of Figure 5.6. During injection period, CO2 rises upward as soon as it is injected into the aquifer because of the strong buoyancy force. After CO2 reaches the top of the aquifer, the upward migration is prevented by the impermeable caprock. CO2 plume starts spreading out under the caprock and flattening away from the injection well. Once CO2 injection ceases, imbibition process occurs to some regions saturated with CO2 before, such as the interface between CO2 plume and pure brine. During this process, water will reinvade into the pore space filled with CO2, and a fraction of CO2 is left behind and trapped as discontinuous phase.

The solution CO2-brine ratio maps that indicate CO2 dissolution in brine are presented in Figure 5.7. During injection period, dissolution happens in regions that are invaded by CO2. During post-injection process, the CO2-rich brine near the well region collapses to the bottom of the aquifer and propagates along it afterwards. Another region that has a very distinctive developing feature is the top CO2 saturated layer. In this region, CO2 leaves the top layer in the form of convective fingers because brine dissolved with CO2 is slightly heavier than pure brine underneath it. As time goes by, those small descending fingerings seem to aggregate and develop into larger fingerings.

The simulation results of converted corner point grid are given by the right plots and compared with the cartesian one. The evolution of gas saturation on cartesian and corner point grid is very similar, while the solution CO2-brine ratio maps show some small differences in fingering behaviors during post-injection period. However, it is mainly resulted from the sensitivity of fingering behavior to the perturbation at the interface, instead of wrong treatment during extension to corner point grid.

The time-lapsed behaviors of different trapping mechanisms on two types of reservoir grid are also compared quantitively in terms of trapping amount. Figure 22 shows the predicted trapping amount due to dissolution, residual trapping and their combination, on corner point grid agree well with the prediction from cartesian grid. Specifically, the dissolution trapping undergoes a substantial growth during injection period. After that, the growth of dissolution slows down and then shows an even larger increase rate at the end of post-injection. On the contrary, only small amount of CO2 is trapped in the residual form during injection period, and there is an abrupt increase after injection stops. However, residual trapping amount starts to decrease after it reaches its maximum during post-injection.

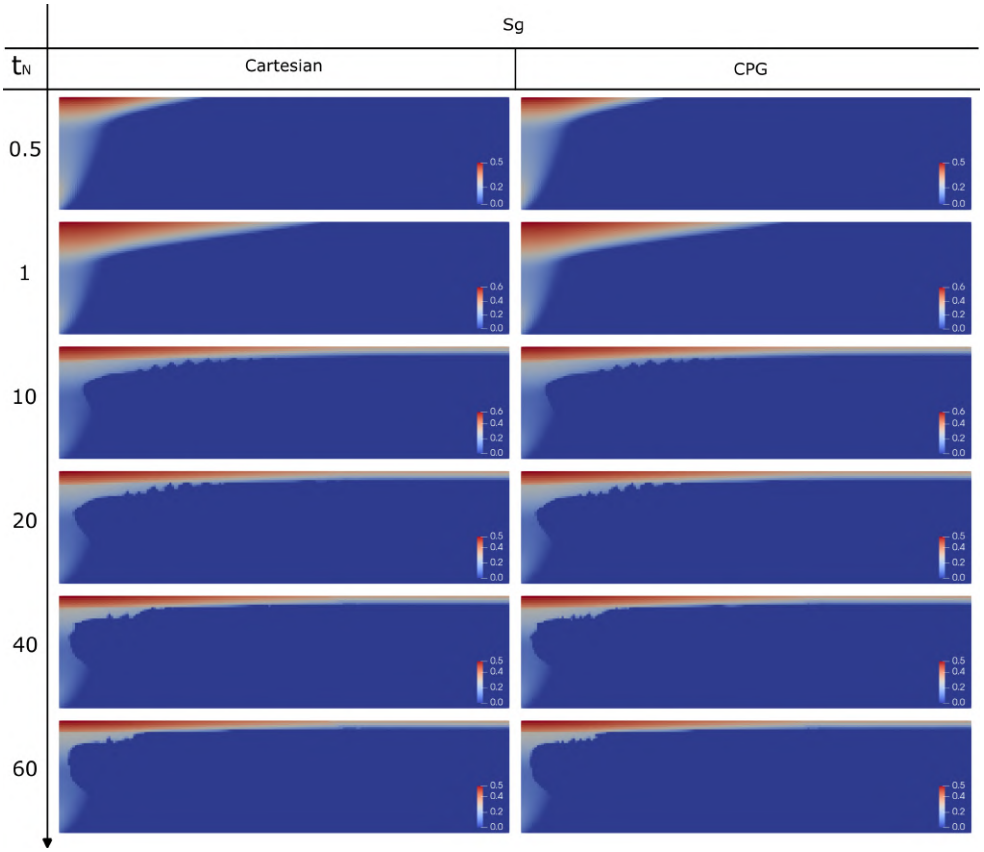

Figure 5.6: Comparison of predicted gas saturation profiles on cartesian and corner point grid.

5.3 3D Cartesian VS CPG

Because dynamic models that are upscaled from geological models normally have a high aspect ratio, another 3D test case is conceived to validate the extended compositional framework to corner-point-grid with such large aspect ratio. Similar to the test case before, the synthetic 3D cartesian box is stored in corner-point format, and simulation on the converted corner-point-grid of the same geometry is conducted afterwards.

The 3D domain consists of 20 x 20 x 10 grid cells, with a grid resolution of 100 m by 100 m by 10 m. As shown in Figure 5.10, the bottom 50 meters of left boundary is perforated to inject CO2, and a production well is placed at the right boundary to allow fluid to flow. CO2 is injected with a rate of 0.05 m3/s for 1200 days. The total simulation time is 252000 days, at which t_N equals to 210. The same physical parameters as before are used. However, it needs to be noted that the relative permeability curves are constructed based on brooks-corey model for better converging properties, while capillarity curves are the same as the 2D case. The only difference from the one used for synthetic 2D case is the curvature of the drainage and imbibition curves for gas phase. The corresponding scanning curve surface is presented in Figure 5.9.

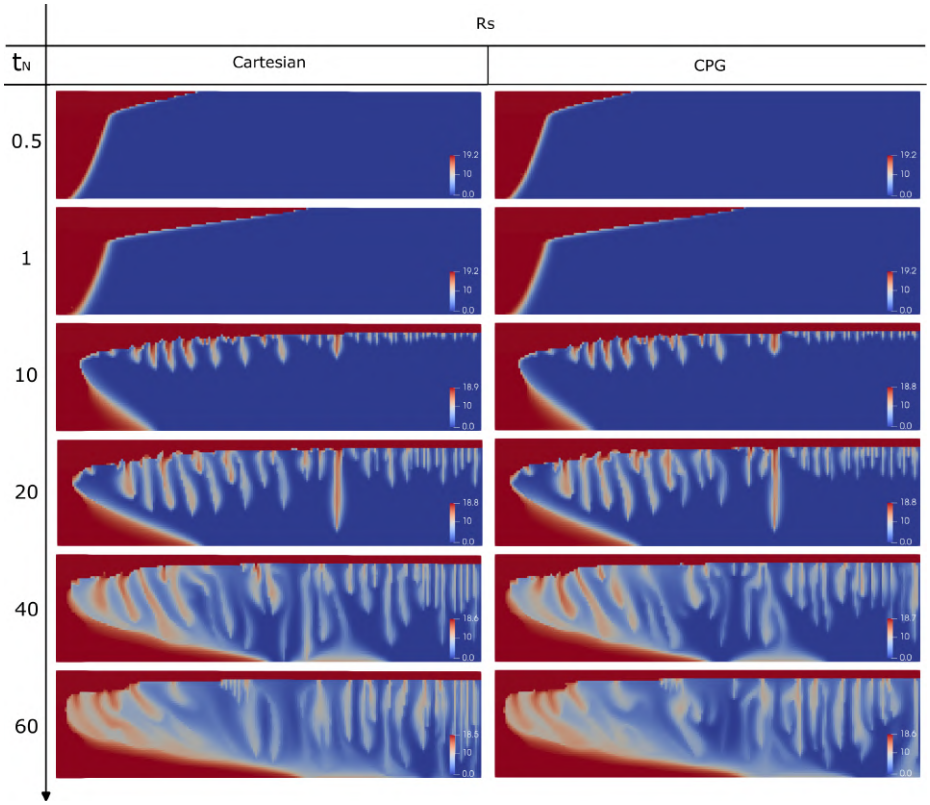

Figure 5.7: Comparison of predicted solution CO2-brine profiles on cartesian and corner point grid.

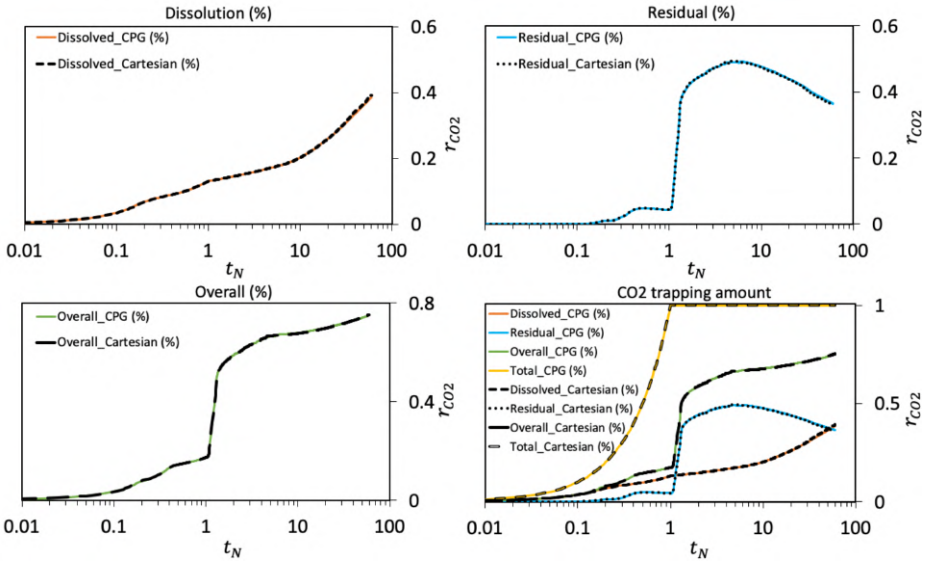

Figure 5.8: Fraction of injected CO2 trapped by different mechanisms on cartesian and corner point grid of the 2D cartesian box model.

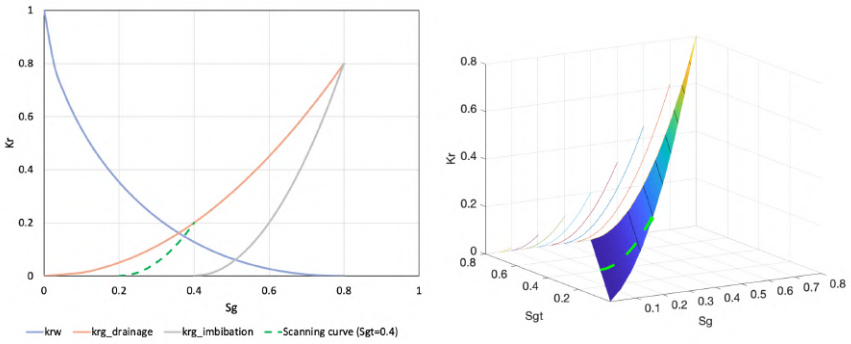

Figure 5.9: Scanning curve surfaces to model the hysteretic behaviors of relative permeability and capillary pressure in field scale test cases.

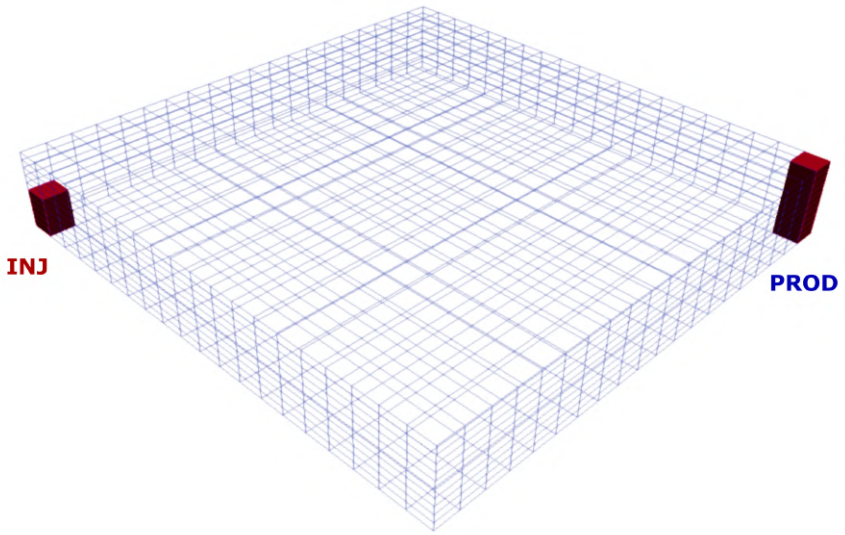

Figure 5.10: Setup of the 3D cartesian box model.

Figure 5.11 shows the injection and migration of CO2 plume in the 3D cartesian box. The simulation results on cartesian and corner-point-gird agree each other very well. The gas saturation at different time steps exhibits a similar displacement trend as the 2D case. CO2 starts migrating upward soon after it enters the pore space. Hindered by the impermeable top boundary, CO2 plume spreads in the top layer as a thin layer afterwards. As given by the solution ratio maps, the dissolution happens as CO2 invading into the pore space. During the post-injection period, the region saturated with CO2-rich brine near well bore slumps away and propagates along the bottom layer, while convective fingers are generated at the interface between the top thin layer filled with saturated brine and pure brine below it.

Figure 5.12 presents the associated dynamic change of trapped amount by various mechanisms, with no obvious difference between the two types of reservoir grid observed. The dissolution trapping shows a relative constant increase rate through the whole process. On the other hand, residual trapping amount remains around zero during injection, while an

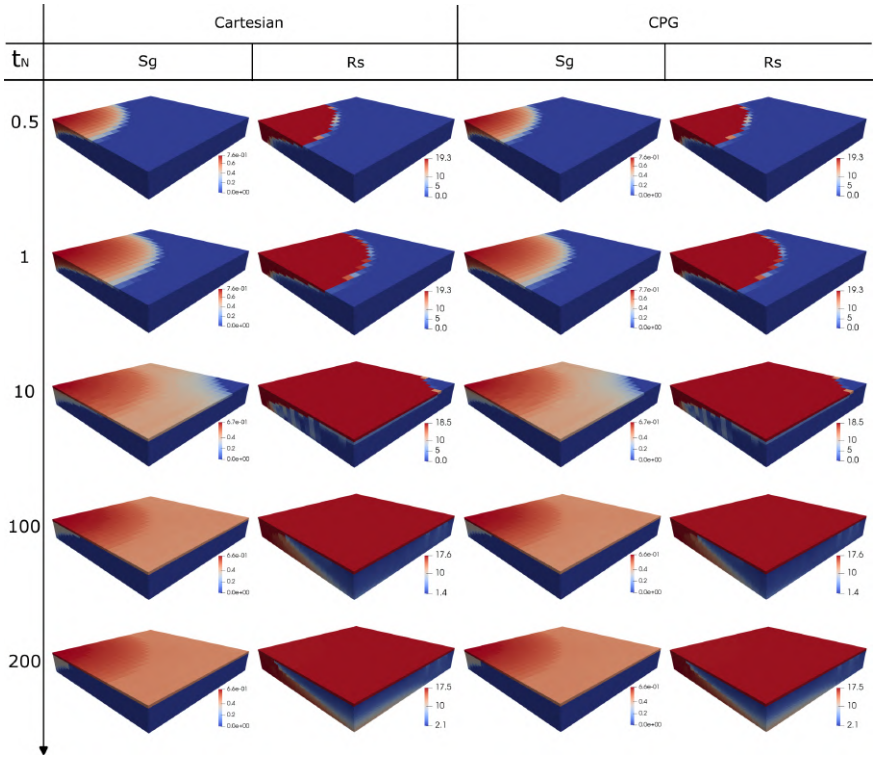

Figure 5.11: Comparison of predicted gas saturation and solution CO2-brine profiles on cartesian and corner point grid.

abrupt increase happens immediately after injection stops. After reaching more than 0.4, the amount of CO2 in residual form starts decrease with a constant rate. The mechanisms behind these dynamic change patterns would be explained later.

5.4 Johansen field

The Johansen formation is a deep saline aquifer of the Sognefjord delta, located about 60 km west of Mongstad area at the south-western coast of Norway, as shown by the geographic map in Figure 5.13. It sits more than 500 meters below the Sognefjord formation, which is the uppermost part of the Sognefjord delta and the main reservoir of the Troll field. The Johansen formation belongs to the lower Jurassic Dunlin Gp and it is located at depth from 2200 to 3100 m below sea level. The formation spreads 60 to 100 km in lateral direction, with an average thickness of 100 meters. As for neighboring geological layers, the Johansen formation is overlaid by thick Dunlin shale in most investigating areas, and it immediately lies above the Amundsen shale [8] [3].

The Johansen formation is regarded as a potential large-scale CO2 storage site due to its sufficient storage capacity, proximity to large point sources and sealing properties. Firstly, the thick deltaic sandstone and wide lateral extension of Johansen formation, confirmed by seismic and well data, provide promising capacity for CO2 storage. In addition, it is

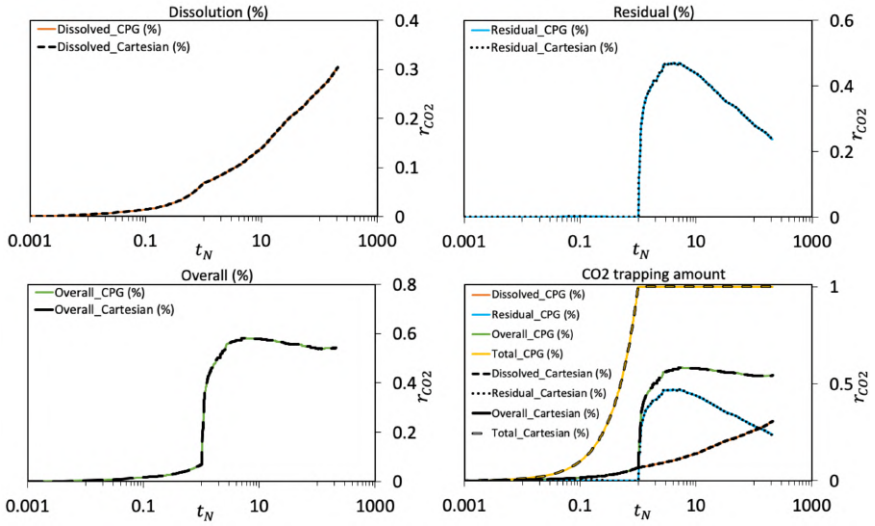

Figure 5.12: Fraction of injected CO2 trapped by different mechanisms on cartesian and corner point grid of the 3D cartesian box model.

found feasible to store CO2 emission from planned power plants at Mongstad and Karsto areas, as indicated by the red dots in Figure 5.13, with pipeline or combined wessel and pipeline solutions. Finally, the neighboring shale layers as aforementioned, particularly the overlying Dunlin shale, ensure the containment of injected CO2. The large capacity of the Sognefjord Delta aquifer above the storage formation also reduces the risk of CO2 leakage to the surface.

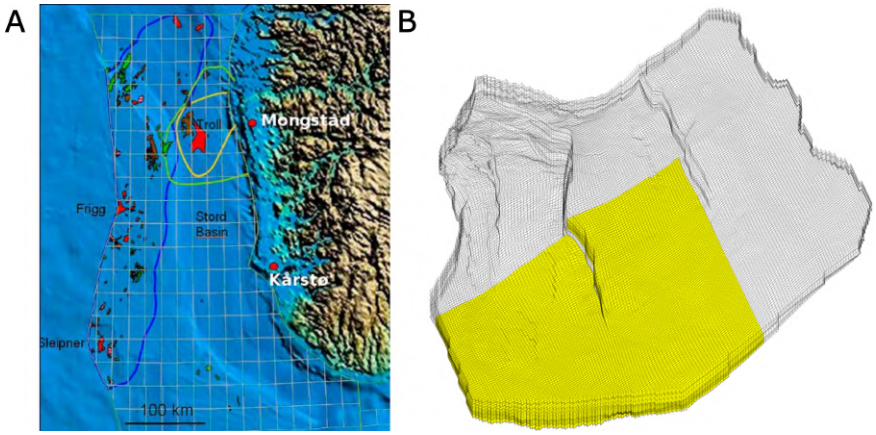

Figure 5.13: Location of Johansen field. (A) Geographic location. (B) Sector model location.

The Johansen dataset, based on available seismic and more than 12 well logs in the MatMoRA project [8], provides an excellent calibration tool for modelling CO2 flow and transport in field scale. The full field model covers all zones and the entire lateral domain mentioned above, consisting of 149x189x16 grid cell. In this study, the sector model focusing on the southwestern part of the geological domain, as shown by Figure 5.13, is used. The sector model has heterogeneous rock properties and is discretized by 100x100x11 grid cells in

NPD5 dataset. However, it needs to be noted that the pinch-out shales in full field model are missing in the sector model because rock properties are interpolated from the geological model and represents a combination of shale and sand properties. Assuming the neighboring shale layers are impermeable, the uppermost five and the bottom layer are not considered, and only the five layers corresponding to the Johansen formation are investigated.

The porosity of Johansen formation is populated with a porosity-depth trend obtained from a neighboring field at equivalent depth level. As shown by the left plot of Figure 5.14, the porosity values range from 0.1 to 0.3. The permeability values are modelled on a basis of porosity-permeability trend from the Sognerfjord formation analogue. The permeabilities in x and y direction are assumed to be the same, while the vertical permeability is ten times smaller than horizontal permeability. The permeability values for the sandstone are mostly larger than 100 mD, as shown by the right plot.

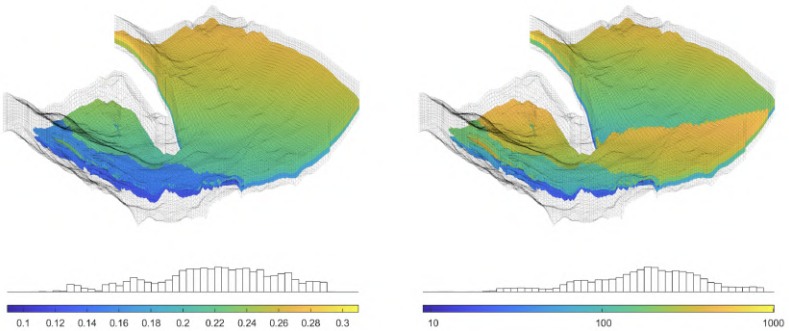

Figure 5.14: Distribution of porosity (left) and permeability (right) in Johansen formation, with sector model outlined by wireframe.

In the proposed compositional framework, thermal effect is neglected, assuming the reservoir is at isothermal condition. The fluid properties at surface condition are same as in the 2D and 3D synthetic cases. CO2 is allowed to be dissolved into the liquid phase, and the density change induced by dissolution and pressure is considered. The dependency of viscosities of different phases on pressure is neglected for simplicity, while an average pressure that the CO2 plume would encounter is used for the constant viscosity values. The fluid properties together with some physical parameters used in the following simulations are summarized in Table 5.3.

Properties	Symbols	Values	Units
Reservoir temperature	T	367.15	K
Initial reservoir pressure @3100m	p_0	310	bar
CO2 viscosity @ 280 bar	μ_{CO_2}	5.65e-5	Pa.s
Brine viscosity @ 280 bar	μ_b	3.88e-4	Pa.s
Injection rate	q	4	Mt/year
Injection time	t_{inj}	100	year
Simulation time	t_{tot}	2000	year

Table 5.3: Physical parameters and simulation scheme of the Johansen test case.

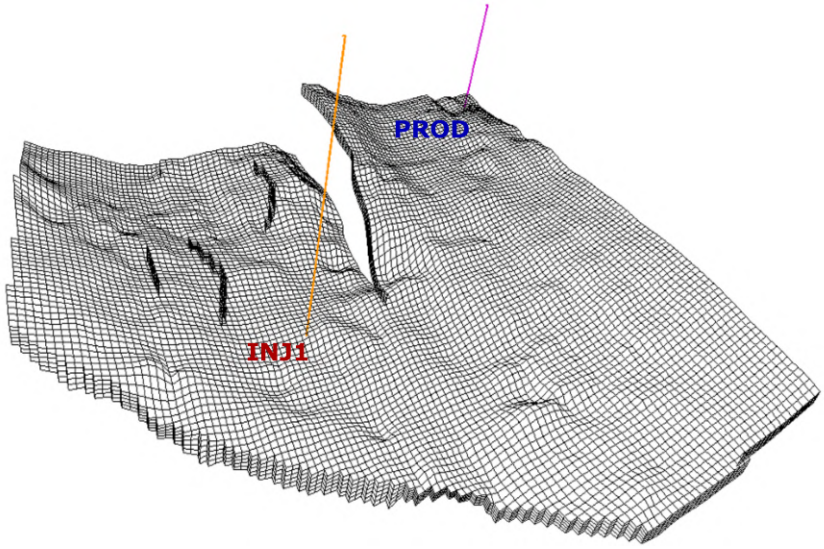

Figure 5.15: Well pattern in the base case.

We assume a No-flow boundary condition, in which the top and bottom boundaries are set impermeable to represent the bounding shale layers above and below. There is no flow happening across lateral boundaries, so the injected CO2 stays in the domain if it reaches the boundaries. A production well is perforated at north-eastern corner to avoid overpressurizing the domain. The injection well is placed at the south-west direction to the major north-south trending fault, which is the deeper part of the domain [2]. The well pattern used in the simulation cases below is given by Figure 5.15.

Assuming a geothermal gradient of $3°C$ per 100m, the reservoir temperature is assumed to be constant at $94°C$ with a surface temperature of $10°C$. The initial pressure in the reservoir is determined by hydrostatic distribution, with a pressure value of 310 bar at reference depth 3100 m. It is suggested that CO2 can be injected at a rate of 4 Mt per year to demonstrate the storage capacity of Johansen formation [8]. In this work, 400 Mt of CO2 is injected into the reservoir over 100 years, after which both injection and production well are shut down. After injection ceases, the simulation continues until 2000 years to predict the migration of CO2 plume and trapping amount during post-injection period.

5.4.1 Physics

The proposed compositional framework incorporates dissolution, hysteresis and capillarity, which are believed to be important for CO2 trapping in saline aquifers. However, to evaluate the relative importance of those physics and better understand the roles they are playing in trapping CO2, a set of simulations in the absence of different physics are compared against the base case, which includes all physics.

The CO2 saturation profiles at different time steps are given in Figure 5.16. Firstly, the base case results are used here to illustrate the evolution of saturation distribution. Since the injection well is placed in the most deep-seated region, CO2 starts to flow upward and does not migrate very far in the lateral direction because of the strong buoyancy force, thus

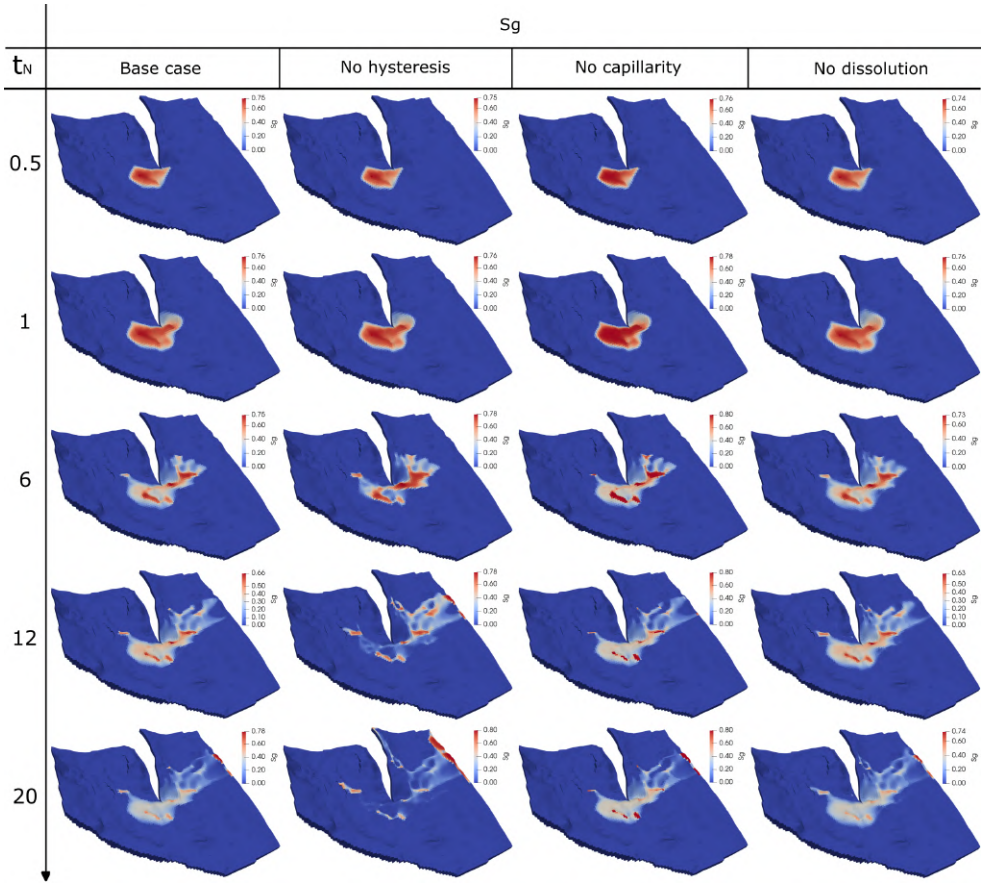

Figure 5.16: Gas saturation profiles for various scenarios in the Johansen field (Base case includes all physical effects).

forming a cone-shape near wellbore region. The upward CO2 plume soon is hindered by the top boundary and spread out in the top layers. At the end of CO2 injection, the plume front reaches the east part of domain and readily migrate to north-east direction further due to the structure dip trend. Dominated by the advective force during injection, the saturation behind the front is relative constant no matter how the depth varies in the top layer. However, only some local domes are filled with high saturation of CO2 after injection stops. This is resulting from the dominating buoyancy force, which drives part of the CO2 at low regions migrate further to northeast direction. At some point before 2000 years, the CO2 plume reaches the eastern boundaries of the domain and is accumulated at those locations.

By neglecting the hysteresis behavior, the same primary drainage curves are used to evaluate the constitutive relations during drainage and imbibition process. It indicates the residual gas saturation is zero, or gas saturation can decrease to zero during imbibition. During injection period, the saturation profiles do not show much difference from the base case because mostly drainage process occurs to the reservoir. The largest difference during post-injection period is gas saturation in most low regions decreases to zero, only leaving some local peak in the migration path filled with CO2. Because more CO2 is free to migrate to the east half from deep regions, the CO2 plume sweeps more areas and even reaches the fault

boundary. In addition, the maximum CO2 saturation occurring to the accumulation areas is larger due to the same behavior.

Following that, we exclude the capillary pressure by equating the pressure in different phases. During injection period, the only obvious difference is the maximum saturation within the plume is slightly larger. Similar to sharpened CO2-brine interfaces due to excluding capillarity in previous study, a sharper interface between local domes that is fully saturated with CO2 and other regions is observed during post-injection.

When neglecting dissolution, we assume that CO2 only exists in gas phase and the compositional flow is simplified to immiscible two-phase flow. In consequence, the solution ratio maps are missing in Figure 5.17, because the amount of dissolution trapping remains zero. As shown by the outline of CO2 plume, the plume front without dissolution propagates further than its counterpart in base case, due to the increase of free CO2 in the absence of dissolution.

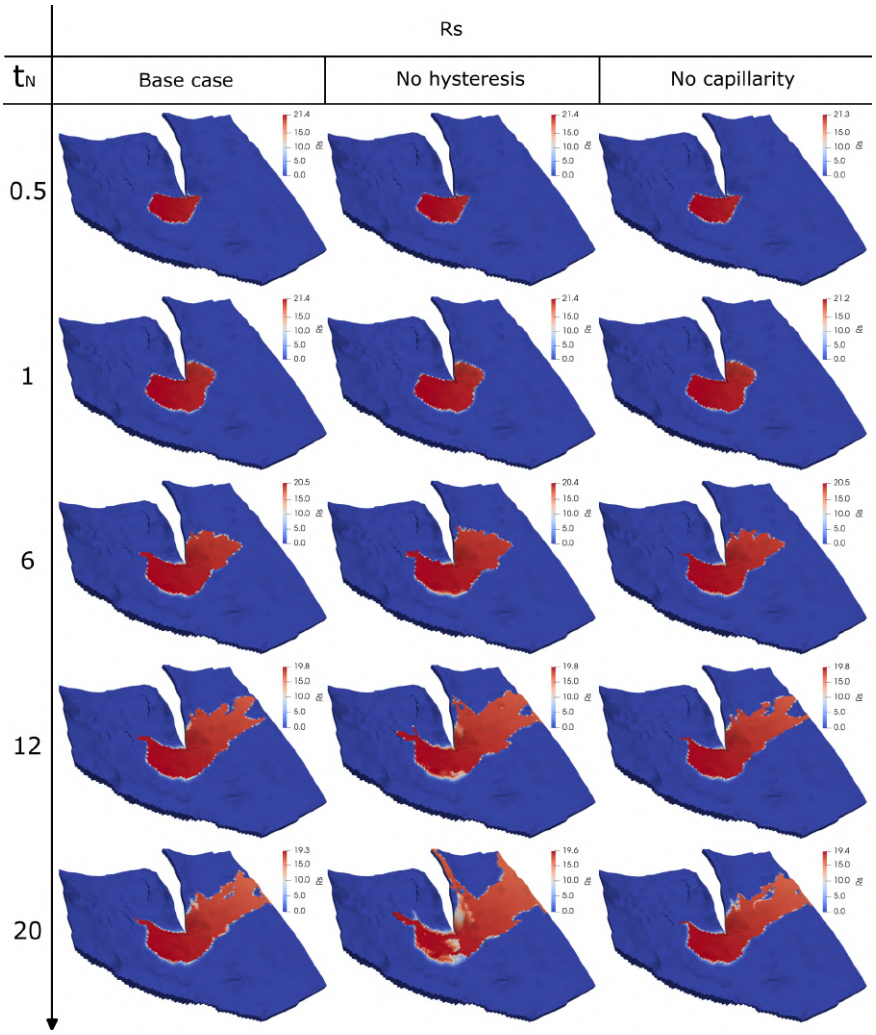

Figure 5.17: Solution CO2-brine ratio profiles for various scenarios in the Johansen field (No dissolution test case is missing because the solution ratio is always zeros).

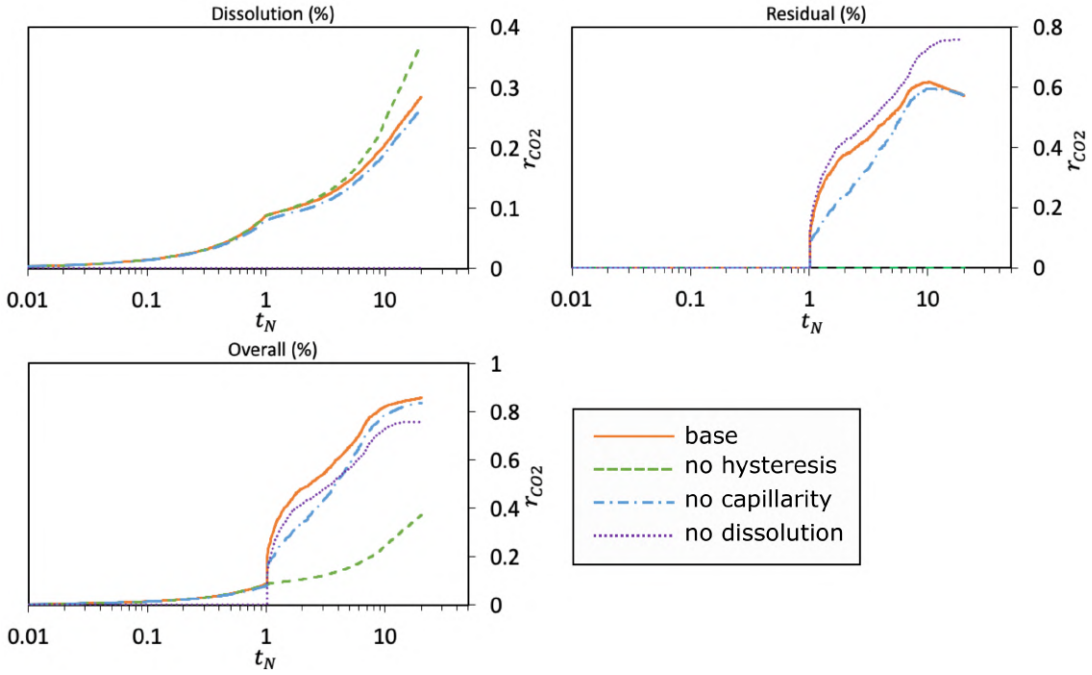

Figure 5.18: Fraction of injected CO2 trapped by different mechanisms for various scenarios in the Johansen test case.

Figure 5.17 shows the dissolution ratio maps at five moments in the absence of different physics. It is clearly revealed that the dissolution happens along the invasion of CO2 plume by the base case results, while the dissolution front is slightly ahead than the plume front in the saturation plot. In addition, it is noted that the solution ratio value gradually decreases towards the eastern boundary since the dissolution limit has a dependency on pressure. In the absence of hysteresis, more cells, particularly cells along the fault boundary, are swept by dissolved CO2 because more CO2 is in mobile state, instead of in residual form. However, neglecting capillarity does not have a big impact on the distribution of solution ratio.

Figure 5.18 shows the fraction curves of trapping amount, and it clearly reveals the different time scales on which various trapping mechanisms act. During the injection period, the rate of the amount of CO2 dissolved in brine gradually increases, while it slows down immediately after injection stops and increases again after some time. However, it is obvious the dissolution plays an equally important role during injection and post-injection periods. On the other hand, the residual trapping amount starts rising rapidly after the cease of injection, until a majority of CO2 is in residual form before the decrease around 1000 years. The fraction curves of overall trapping indicate the structural trapping plays a decreasing role while the residual and solubility trapping become more important along time.

As for the case neglecting dissolution, the amount of residual trapping also has the feature of rapid increase after injection stops. Another important difference is the maximum fraction it reaches is even larger than that of the base case, and it remains constant afterwards. The larger fraction value is resulted from the further front position of CO2 plume at same time and a larger swept area due to the absence of dissolution. In addition, the unchanged residual trapping amount after its maximum is because the convective transport, driven by

density difference between brine dissolved with CO2 and pure brine below it, is missing. Those descending fingers observed in base case can cause a shift of constitutive relations, such as from scanning curve back to primary drainage curve. In the case without dissolution, the residually trapped gas can no longer be released as in base case, and the amount remains the same.

When removing capillarity, the amount of dissolution trapping agrees well with base case during injection, except a minor deviation of starting from $t_N = 0.2$. This deviation causes a slightly smaller fraction of CO2 dissolved in brine at the end. It is because the higher saturation in invading zone leads to a smaller swept area. The dynamic change of residual trapping amount shows a similar pattern as base case, which can prove that an interplay between hysteresis and dissolution trapping exists. However, a slower decreasing rate is observed at the end. It can be inferred that the convective transport during post-injection is impacted by the balance between capillary and buoyancy force. The existence of capillary pressure can help brine be imbibed into top gas cap, and CO2 can leave the top layer in the form of descending fingers.

In the absence of hysteresis, the amount of CO2 in residual form is zero all the time because residual gas saturation decreases to zero. The amount of dissolved CO2 during injection does not show much difference from the base case, while a significant larger fraction of CO2 is trapped in dissolution form during post-injection period. This difference is resulted from larger swept areas without residual trapped CO2.

5.4.2 Linear trapping model coefficient

A scanning curve starts from the turning point (S_{gt}), from which the transition between drainage and scanning curve happens, and it ends at corresponding residual gas saturation $(S_{gr}\ \ (S_{gt}))$. The residual gas saturation point is corresponding to a specific scanning curve, and it is determined with a linear trapping model as [26]:

$$S_{gr} = f_r S_{gt} \tag{5.1}$$

In which f_r is a linear coefficient to decide how much fraction of CO2 would be in residual form if a cell is transitioned to imbibition process with a saturation S_{gt}.

However, the impact of this linear coefficient on residual trapping and its indirect impact on dissolution trapping are not clear. In this study, three different linear coefficients are used to investigate how the evolution of saturation and solution ratio are impacted. Figure 5.19 shows the difference in saturation profiles caused by different linear coefficients. During post-injection, less CO2 is in residual form as shown by the low saturation value in the same migration path as the coefficient decreases. In consequence, more mobile CO2 can migrate along the topology of the top layer to shallower regions, which can be seen from the swept cells near the fault. In addition, the solution ratio maps in Figure 5.20 also indicate that an increasing number of cells are invaded by CO2, as f_r decreases from 0.5 to 0.1.

As given by Figure 5.22, the extra dissolved CO2 with smaller f_r is due to a larger swept area. Although a similar pattern is observed by the three fraction curves of residual trapping, the amount of CO2 in residual form at the end heavily depends on the investigated linear coefficient. The residual saturation profiles given in Figure 5.21 clearly reveal that the largest residual saturation values are scaled by the linear trapping coefficients. In other words, less CO2 would be eventually trapped in residual form with a smaller f_r, if the process turns to imbibition at a same saturation value.

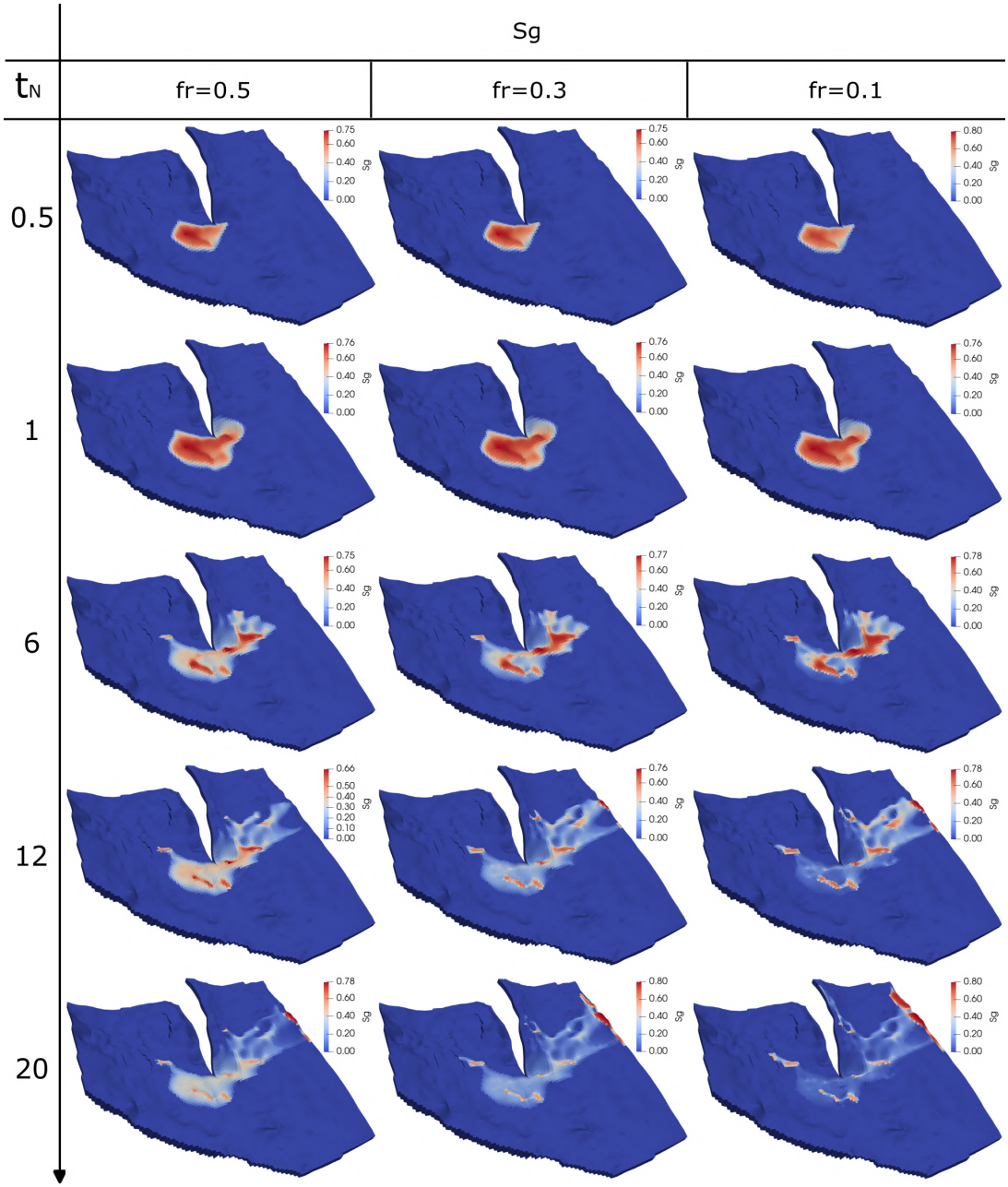

Figure 5.19: Gas saturation profiles in the top layer of Johansen field with different linear trapping coefficients.

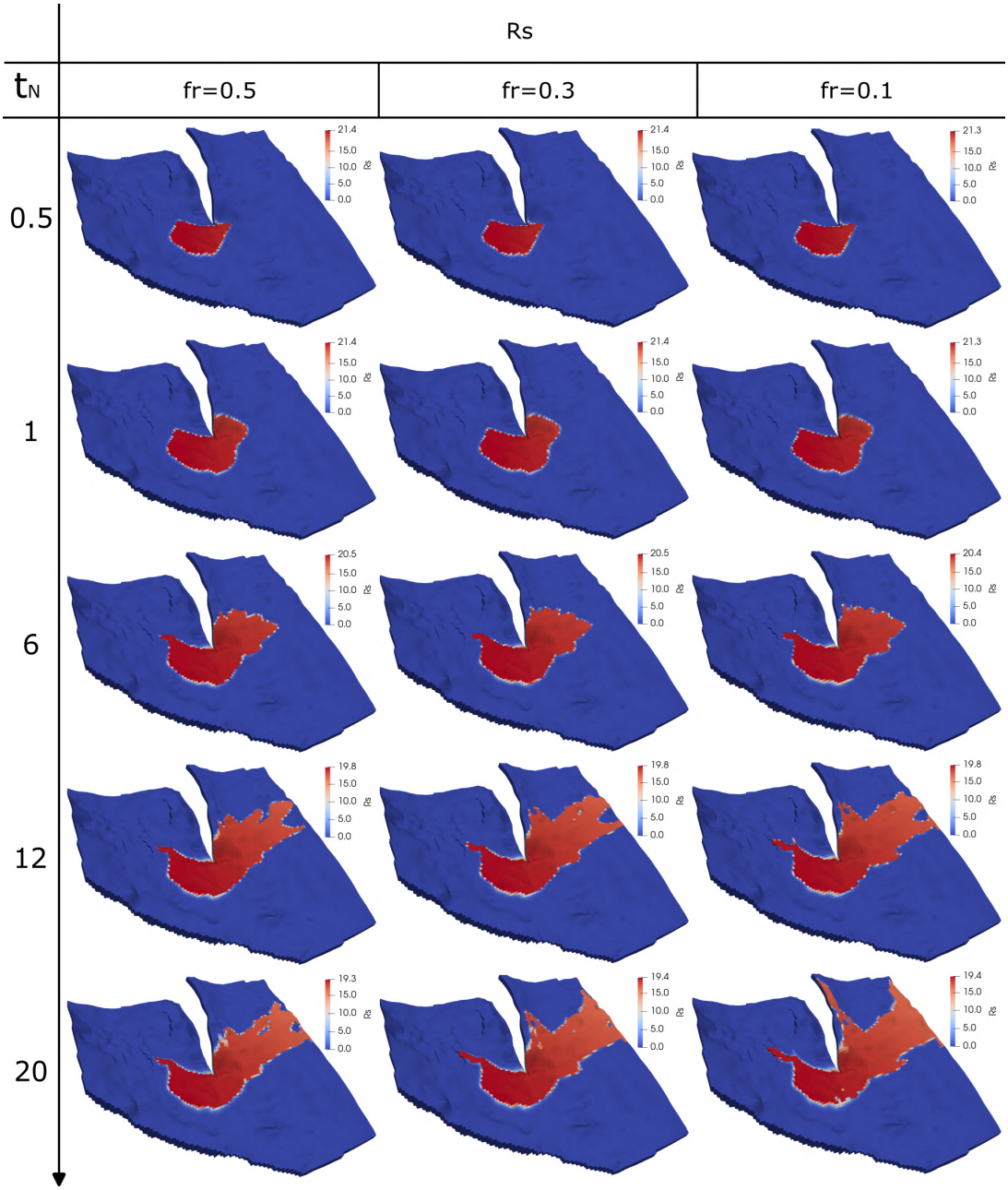

Figure 5.20: Solution CO2-brine ratio profiles in the top layer of Johansen field with different linear trapping coefficients.

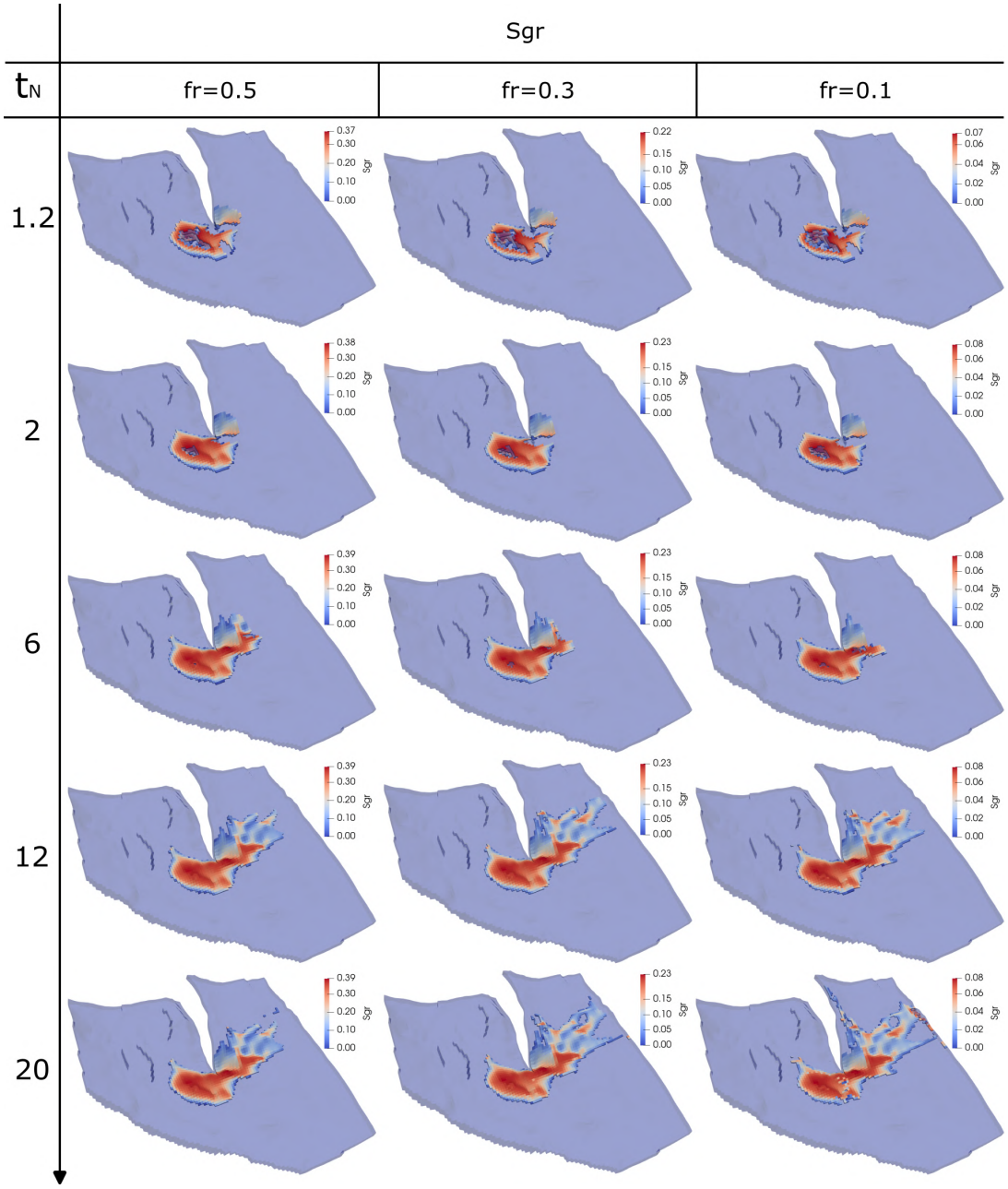

Figure 5.21: Residual gas saturation profiles in the top layer of Johansen field with different linear trapping coefficients.

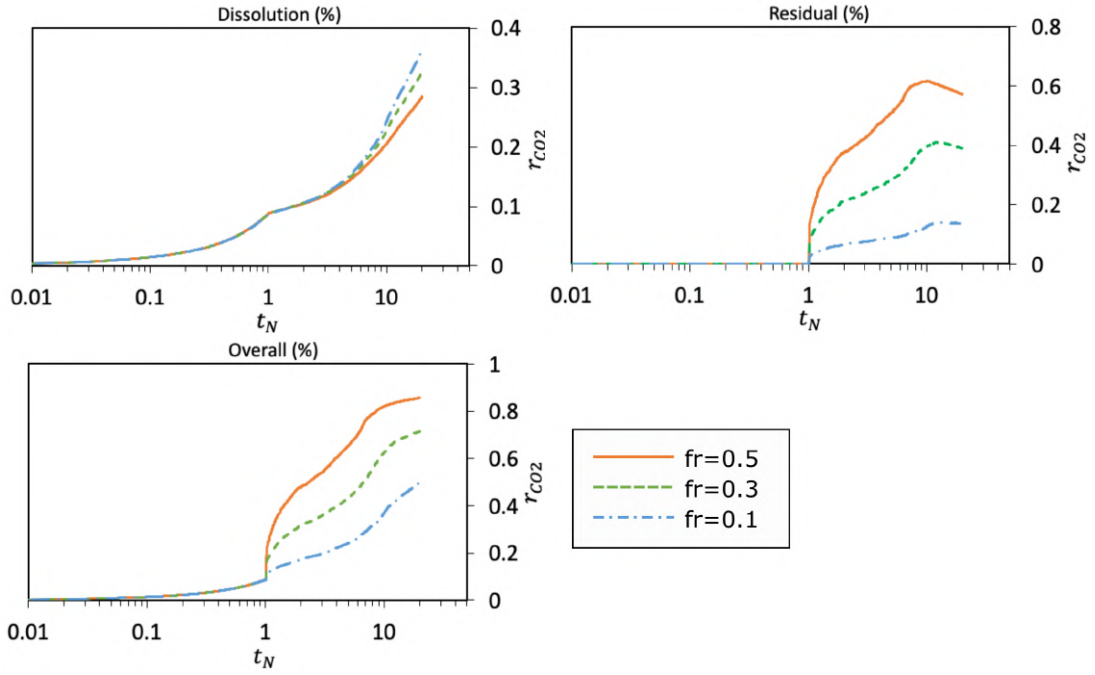

Figure 5.22: Fraction of injected CO2 trapped by different mechanisms with different linear trapping coefficients.

Well index	x [m]	y [m]	i-index	j-index	k-index
INJ1	524276	6692948	57	47	6-10
INJ2	520847	6693306	64	47	6, 7, 10
INJ3	521139	6696877	64	40	6, 7, 10
PROD	555553	6714358	1	1	6-10

Table 5.4: Coordinates of injection and production wells.

5.4.3 Injection location

In this work, three injection scenarios are simulated to examine the change of migration path and how trapping amounts differ from each other if different migration path is taken. Furthermore, an optimized location for the injection well can be proposed based on predicted trapping amount. The coordinates for proposed injection wells and the producer are summarized in Table 5.4. The location of well INJ1 is same as the base case before, and all 5 layers are perforated for injection. The well INJ2 is 3km west to the proposed INJ1, while the well INJ3 is 3km north to INJ2, as shown in Figure 5.23. It needs to be noted that only layer 6, 7 and 10 are perforated around INJ2 and INJ3 to ensure injectivity because there is a low-permeability wedge existing in the other two layers.

The distribution of gas saturation and solution ratio in the top layer are given in Figure 5.24 and Figure 5.25 respectively. It is noticed that slightly more CO2 migrates to north in the well INJ2 scenario, while a small fraction of CO2 still reaches the east boundary after 2000

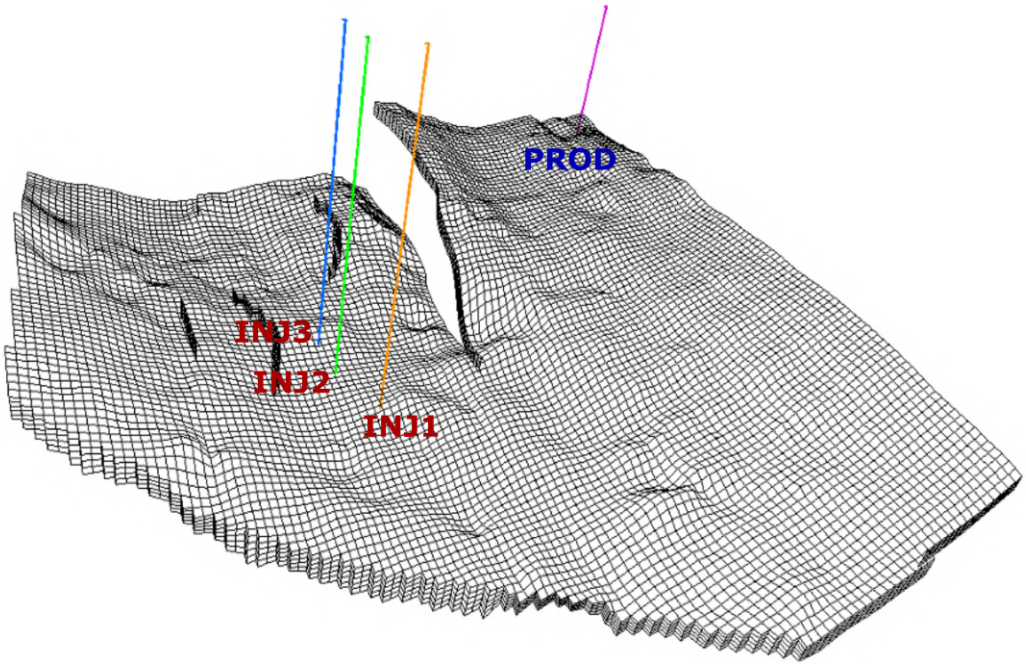

Figure 5.23: Well patterns in the sensitivity study on injection location.

year. In comparison, most CO2 migrates and stays in the west half at the end of simulation when CO2 is injected through well INJ3.

Figure 5.26 shows the increase rate of dissolution trapping amount in the well INJ1 case is slightly slower than that of the other two cases. It is inferred that the pressure in the regions around the well INJ2 and INJ3 increases faster because a larger injection rate is imposed when same amount of CO2 is injected through only three sources. Because the dissolution limit is proportional to pressure at given temperature, slightly more CO2 can be dissolved into brine in these two cases.

However, the residual trapping amount reduces by more than 0.1 in both well INJ2 and INJ3 cases, following a similar development pattern as the well INJ1 case. This difference is partially because less CO2 is in gas phase while more dissolution occurs. Moreover, as given by Figure 5.27, the distribution of gas and residual gas saturation reveals that significant amount of free CO2 still exists in the bottom layer of the two cases, due to the bounding low permeability wedge and impermeable bottom boundary. These two effects reinforce each other and cause the reduction of residual trapping in the INJ2 and INJ3 cases. Moreover, overall trapping plays a less important role in the last two cases, as indicated by the reduction by around 0.2 at the end of simulation.

5.4.4 Depth

The density of CO2 changes abruptly at around 800 meters depth because of the change from gaseous to supercritical CO2. This sensitivity study is designed to investigate the trapping potential of aquifers at different depth and how the various trapping mechanisms

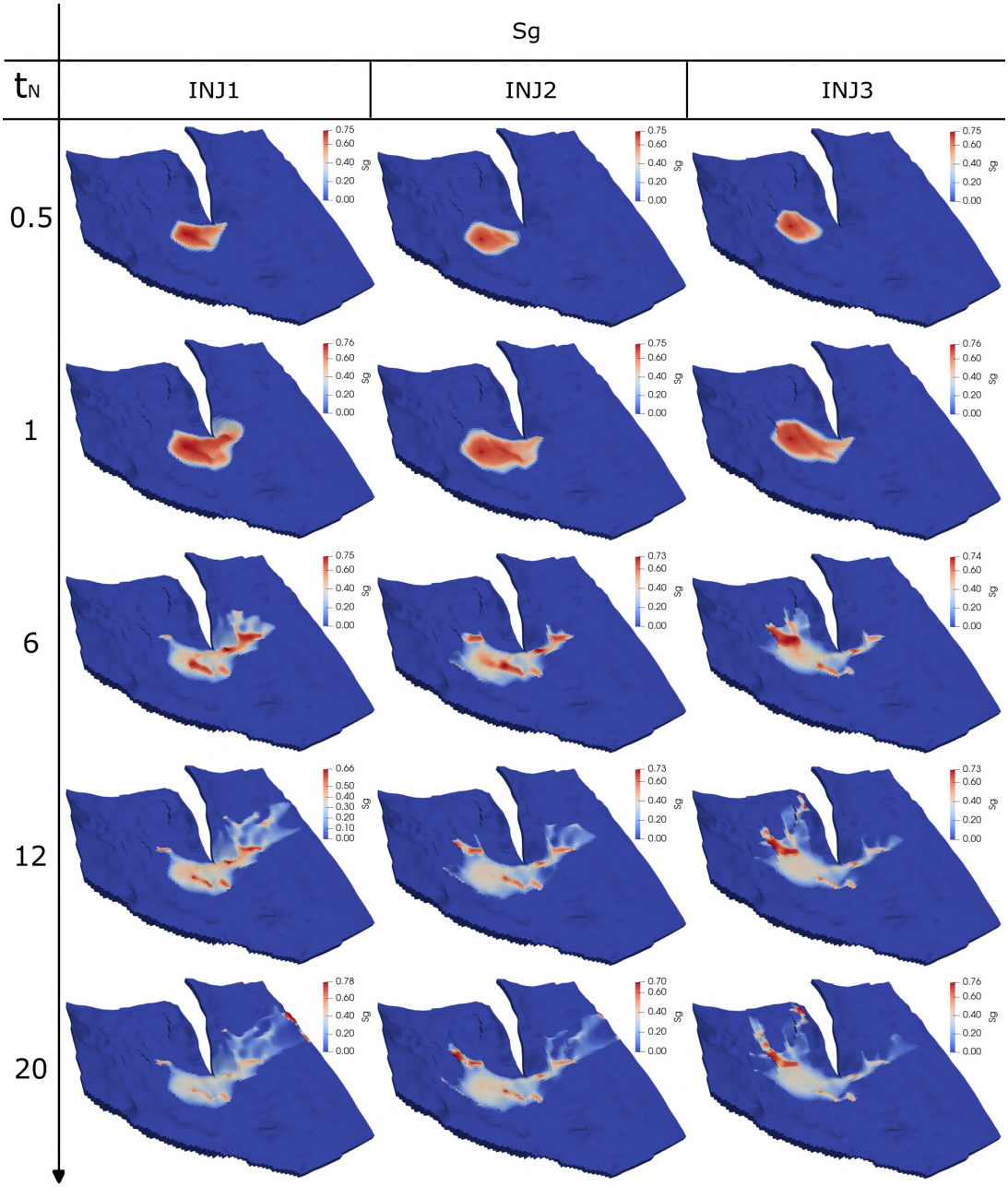

Figure 5.24: Gas saturation profiles in the top layer of Johansen field with different well patterns.

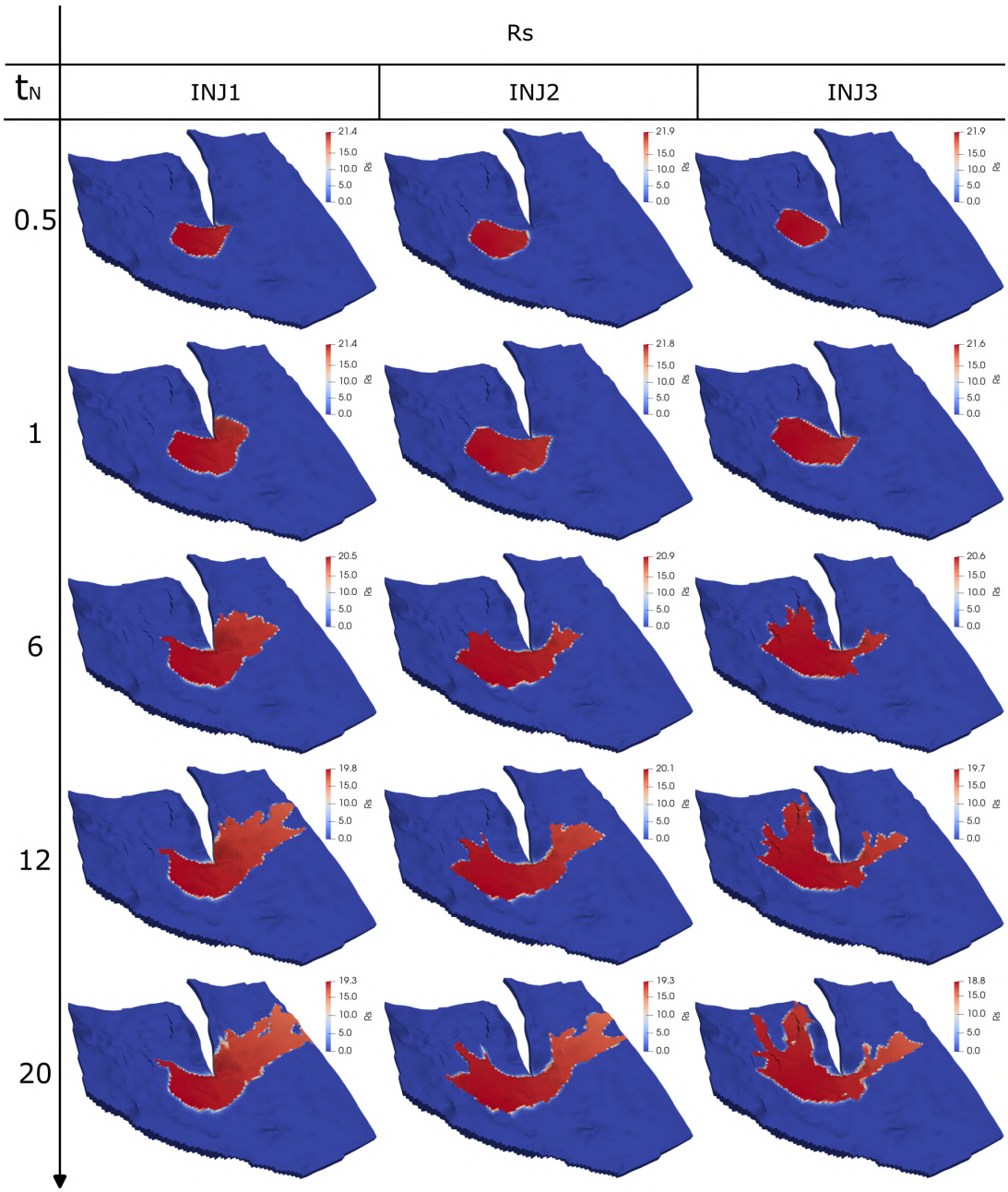

Figure 5.25: Solution CO2-brine ratio profiles in the top layer of Johansen field with different well patterns.

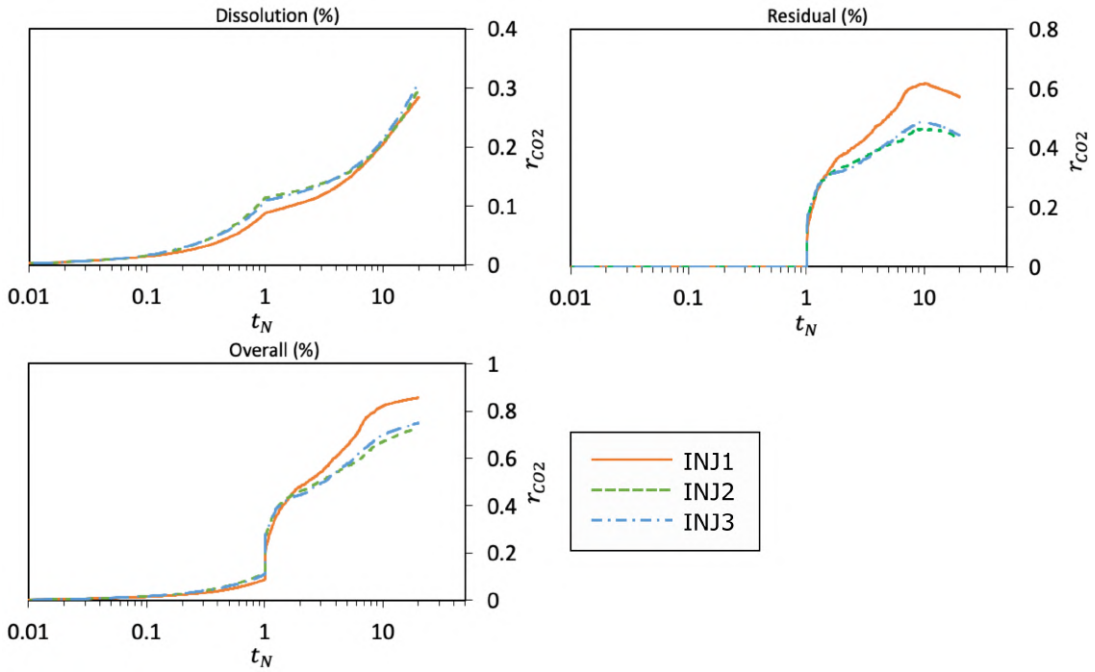

Figure 5.26: Fraction of injected CO2 trapped by different mechanisms with different well patterns.

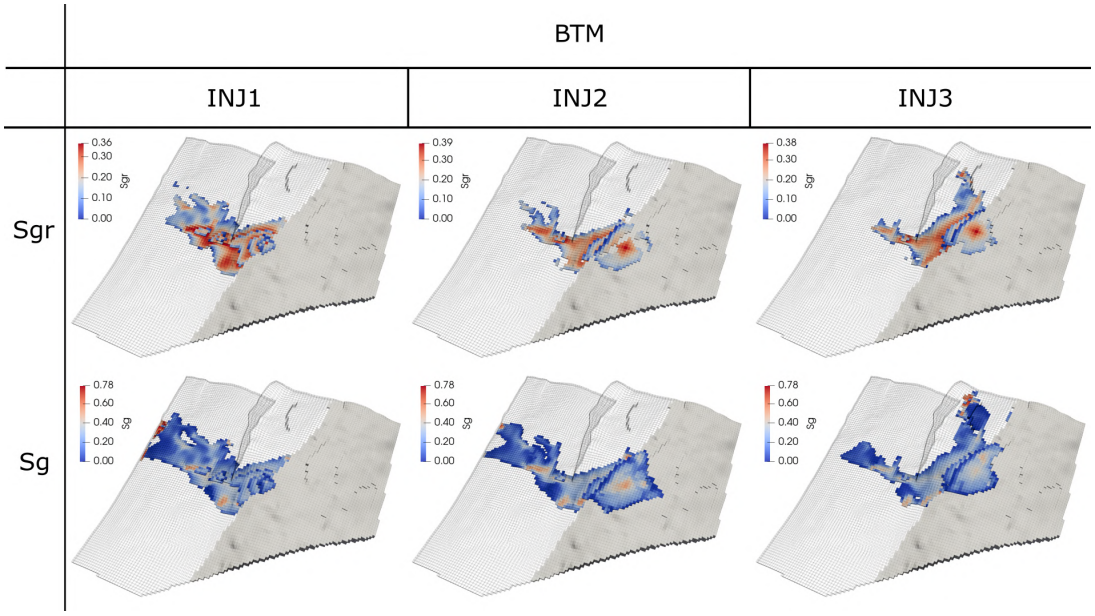

Figure 5.27: Residual gas saturation and gas saturation in the bottom layer of Johansen field after 2000 years. Solid cells represent the location of low-permeability wedge in the west of the field, while wireframe represents the outline of the field.

Depth [m]	Temperature [°C]	CO2 viscosity [Pa.s]	Brine viscosity [Pa.s]
2800	94	5.65e-5	3.88e-4
2000	70	5.39e-5	5.13e-4
1200	46	4.99e-5	7.41e-4

Table 5.5: Physical parameters of fluids in the sensitivity study on aquifer depth.

act differently. An average depths can be obtained from the interval in which CO2 plume migrates. We conceive two other scenarios at different average depths, based on which the temperature and viscosity of fluids are determined. In other words, the same reservoir grid is used, while the reservoir as whole is assumed to be at shallower depth. Table 5.5 summarizes the parameters used in different simulation cases.

Figure 5.28 and Figure 5.29 show the saturation and solution ratio maps respectively. The first two cases do not show much difference, which is resulted from the small density difference between the two cases as shown in Figure 5.30. However, the plume front in the case with the shallowest depth propagates less further during post-injection period, comparing with the first two cases. It is inferred that the buoyancy force in the third is not as large as the first two cases, which means that the density of CO2 is slightly larger than that of the first two cases during the later stage of migration.

Figure 5.31 shows the fraction curve of trapping mechanisms in different cases. The third case has slightly more CO2 dissolved in brine because the solubility limit is larger as shown in Figure 5.29. However, the dissolution in the other two cases exceeds it during post-injection because of larger swept area. The same reason also causes less CO2 in the residual form at the end, although a similar growth pattern is observed.

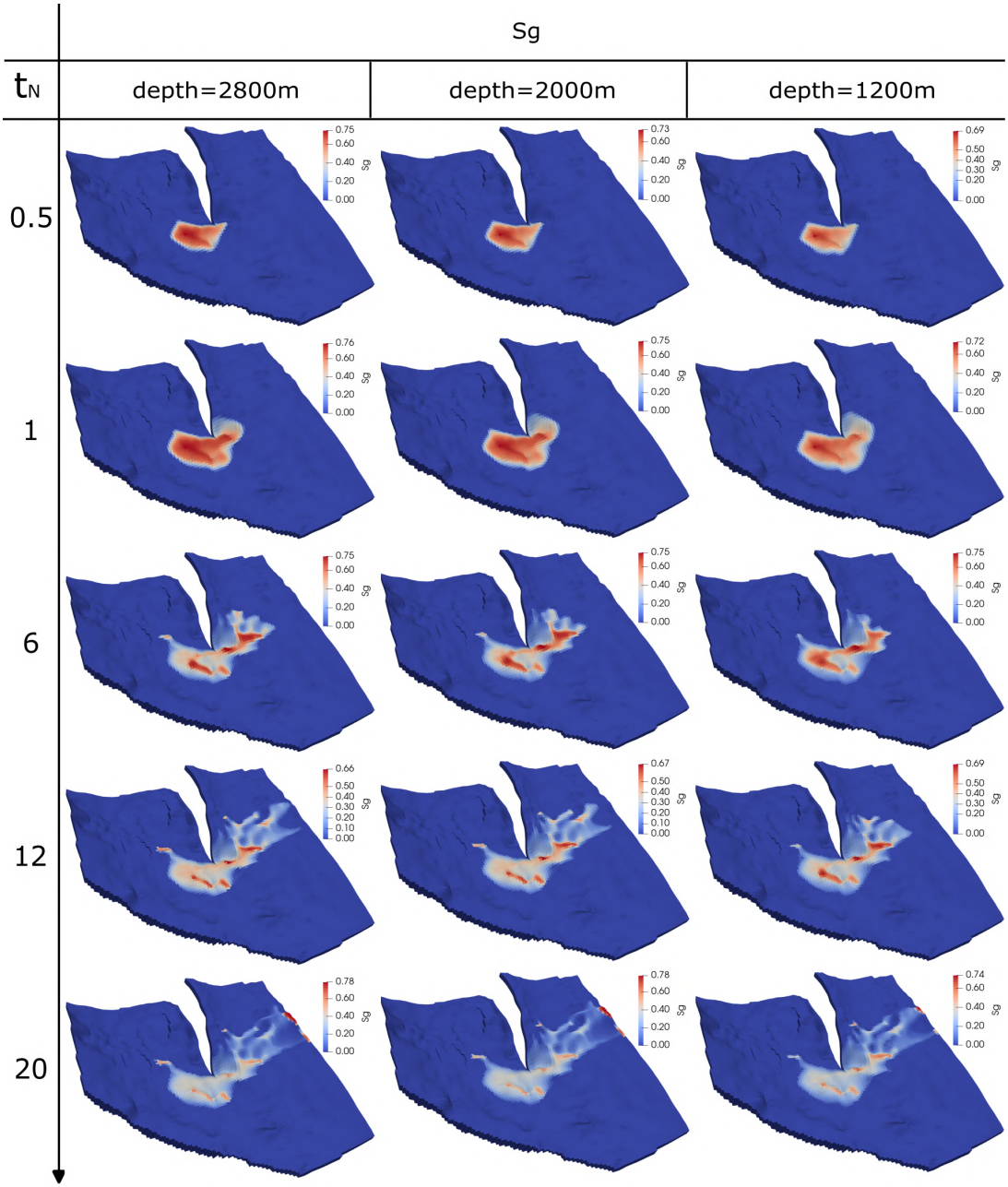

Figure 5.28: Gas saturation profiles in the top layer of Johansen field in different aquifer depth scenarios.

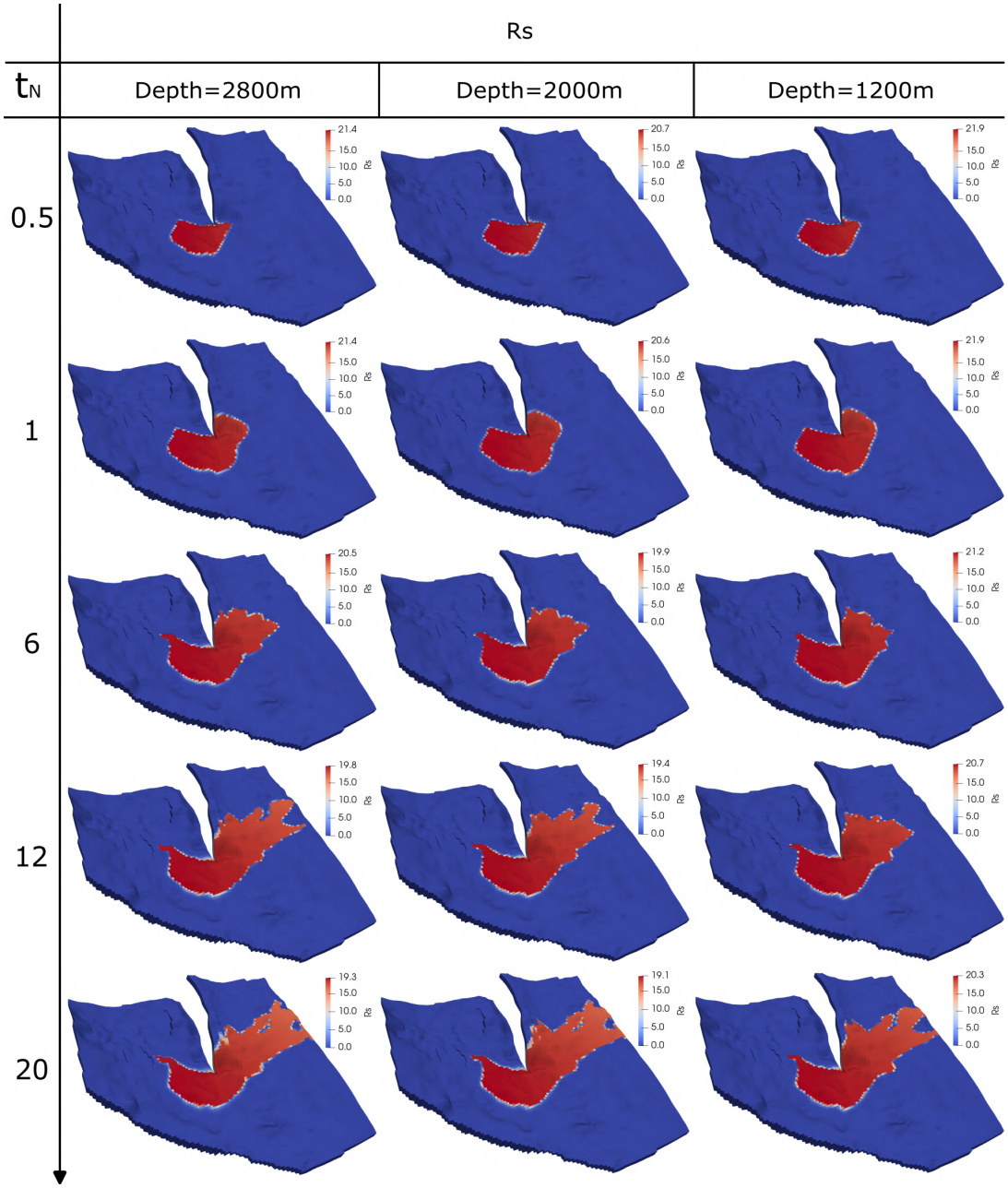

Figure 5.29: Solution CO2-brine ratio profiles in the top layer of Johansen field in different aquifer depth scenarios.

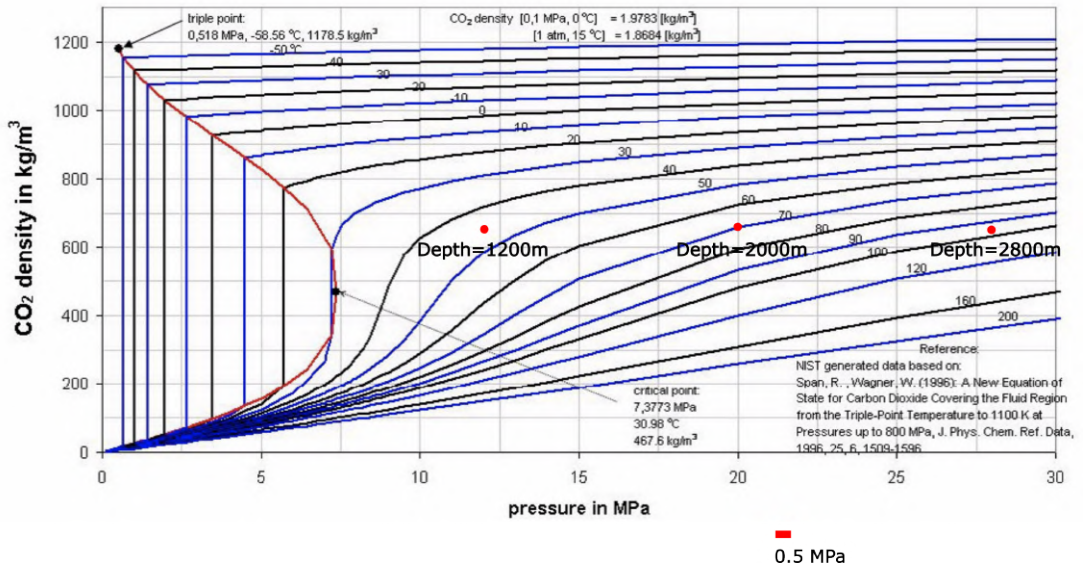

Figure 5.30: CO2 density under the average reservoir pressure in different aquifer depth scenarios [30]

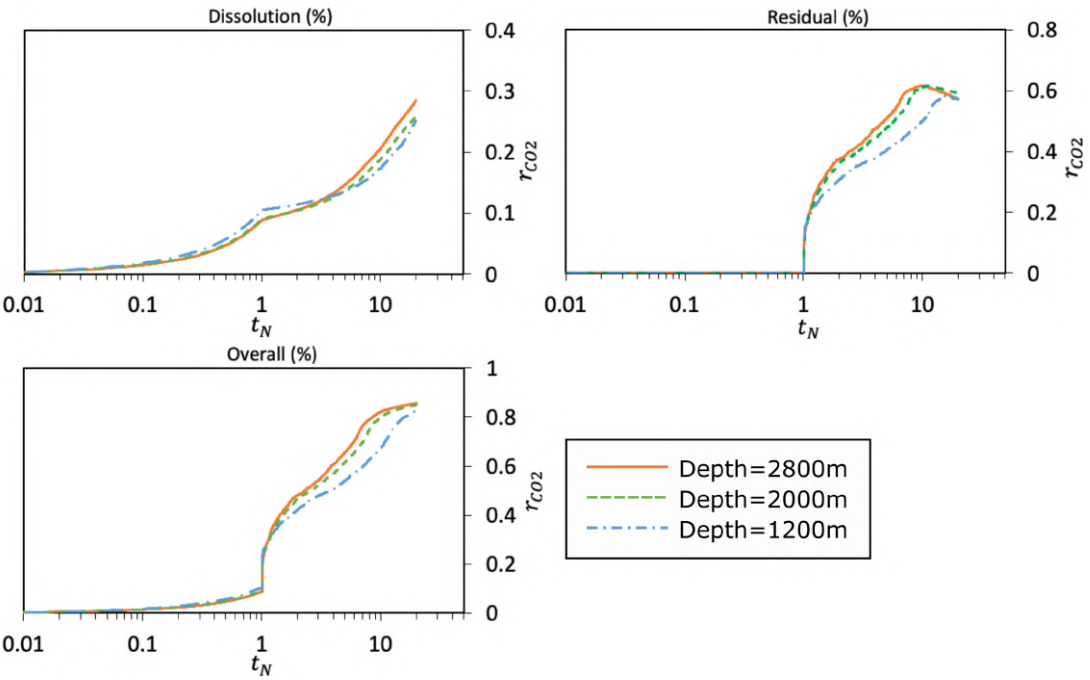

Figure 5.31: Fraction of injected CO2 trapped by different trapping mechanisms in different aquifer depth scenarios.

6 Conclusions

In this work, we present a compositional framework that is developed to simulate CO2 storage during lifelong process in saline aquifers with complex geological features based on corner point gird geometry. The general framework that considers various physical effects, improves computation efficiency by a parameterization method.

The proposed compositional framework is evaluated by several test cases focusing on its different capabilities. The benchmark problem, in which CO2 is injected in a layered formation, demonstrates the ability of the simulator to describe the key processes happening in viscous to gravity driven flow. The well captured phenomena, such as CO2 accumulation under capillarity barriers, gas breakthrough and dissolution, validates that these physical effects are reliably considered. In the followed 2D and 3D test cases, the reliability of the extension work to corner point grid is examined. Following that, the roles of various physical effects are playing in trapping CO2 are investigated in a realistic reservoir model. Moreover, the sensitivity of the migration of CO2 plume and trapping amount on well patterns and other physical parameters are studied. Here below are the main findings from the field study.

6.1 Roles of different physics

The dissolution of CO2 in brine occurs when CO2 and brine are in contact. As CO2 migrates and spreads in top layer, the brine dissolved with CO2 tends to sit on the top of pure brine, which leads to gravitational instability. Eventually, this would trigger the convective transport from plume above to the bottom of aquifer. It is found that an interplay between dissolution and hysteresis exists as the convective displacement may shift constitutive relations and release residually trapped CO2 furthermore.

The hysteresis behavior of constitutive relations means that they do not only depend on the current saturation value, but also the saturation history or the process that is taking place. In our framework, a scanning curve surface, or a parameterized space, can be constructed based on primary bounding curves. Knowing a pair of saturation value and turn point corresponding to that specific cell, constitutive relations can be determined directly from the obtained space. Moreover, the unique residual saturation corresponding to every cell on different scanning curves can also be modelled. In this way, the effect of residual saturation, one of the most important trapping mechanisms, is captured in a robust way.

Capillary force can help imbibe brine into the part of aquifer occupied by CO2, by which a transition zone from the plume to pure brine below is formed. In the transition zone, gas saturation value decreases from CO2 endpoint saturation to zero. Thus, the existence of capillarity would have an impact on saturation values in the plume and total swept area, through which the dissolution and residual trapping amount are affected. Moreover, it is inferred that the convective transport during post-injection period is accelerated while

capillarity exists, indicated by the larger decrease rate of residual trapping at the end in base case.

6.2 Dynamic change

The fraction curves of trapping amount by various mechanisms indicate that the identified trapping mechanisms operate on a variety of time scales. In particular, the increase rate of dissolution trapping amount often changes after injection stops, but the trapping contribution is found equally important during injection and post-injection period. On the contrary, residual trapping often starts playing a role after injection stops, while its contribution can surpass that of dissolution trapping in a short time. At the late stage, obvious evidence shows that the two trapping mechanisms interact with each other and cause a decrease of the trapped amount in residual form.

6.3 Trapping amount of different mechanisms

In the field scale study, around 10% of trapped CO2 is attributed to dissolution trapping with a constant rate during injection. At the end of simulation, the amount of dissolution trapping increases to around 30%. However, the increase rate during post-injection period tends to slow down and increase again after some time. On the other hand, the amount of CO2 in residual form almost remains zero during injection because drainage process is dominating in the invaded pore space. Immediately after the cease of injection, an abrupt increase in residual trapping amount is observed, which can be attributed to the invaded regions around injection well. The trapped amount starts to decrease with a relatively slow rate after it reaches the maximum values. The decrease is resulted from the release of residually trapped CO2 by the descending fingers.

The sensitivity study on well pattern reveals that the amount of dissolution trapping is sensitive to pressure change, while residual trapping amount can be impacted by the rock heterogeneity. The existence of low-permeability wedge increases the contributions of structural or stratigraphic trapping since a significant amount of free CO2 is trapped below some local structural features. However, the residual trapping amount is reduced because less CO2 can migrate and get residually trapped along the migration path. On the other hand, the amount of residually trapped CO2 heavily depends on the linear coefficient that is used to model residual gas saturation effect. The trapping potential of aquifers at different depths do not show much difference in these conducted scenarios. However, it is partially due to the limitation of assumed isothermal condition and constant viscosities, without which the different behaviors of CO2 plume caused by depth change are expected to be better captured.

7 Future work

The developed compositional framework demonstrated its predictability on plume migration and trapping amount in the application to a field-scale reservoir grid. In this section, some topics for further improvements are suggested.

7.1 Thermal effect

In this study, thermal effect is neglected by assuming an isothermal condition. However, CO2 is normally expected to migrate over large distances, which normally corresponds large elevation and temperature difference in realistic reservoir. Non-isothermal effects play a significant role in CO2 injection and plume migration due to thermodynamic equilibrium and fluid properties [31]. Moreover, it is found that mechnical risks, such as casing failure, may increase due to thermal stresses caused by temperature difference between the wellbore and the surrounding rock [29]. Thus, to capture the migration of plume and assess trapped amount more accurately, energy balance equation needs to be introduced to address the coupled thermo-hydro-mechanical-chemical problem.

7.2 Molecular diffusion

Molecular diffusion is suggested to be considered by some research because CO2 storage in saline aquifer normally happens on a century-long time scale, on which it can be an important factor [13]. For example, dissolved CO2 in brine is transported away from the interface of the two phases driven by diffusion, although it is believed to be an extremely slow process. To incorporate the physical effect of diffusion, a non-advective flux of one component within a given phase needs to be introduced into the mass conservation as [9]:

$$\frac{\partial}{\partial t}\left(\phi\rho_T z_c\right) + \nabla \bullet \left(\sum_{\alpha=1}^{n_{ph}} x_{c,\alpha}\rho_\alpha u_\alpha\right) + \nabla \bullet \left(\sum_{\alpha=1}^{n_{ph}} S_\alpha \rho_\alpha J_\alpha\right) - \sum_{\alpha=1}^{n_{ph}} x_{c,\alpha}\rho_\alpha q_\alpha = 0,\ \forall c \in 1,\ ..,n_c \quad (7.1)$$

in which J_α is the diffusion flux of component c in phase α. According to Fick's law, it is proportional to its concentration gradient as:

$$J_\alpha = -\phi D_{c,\alpha} \nabla x_{c,\alpha} \quad (7.2)$$

where $D_{c,\alpha}$ represents the diffusion coefficient for component c in phase α.

7.3 pEDFM implementation

The widespread fractures in subsurface geological formations, which are naturally and artificially induced, can have significant impact on flow patterns, because of the large contrast in conductivity between fractures and their neighboring host rock. The projection-based embedded discrete fracture model (pEDFM) can be implemented to represent fractures explicitly and investigate the role of fractures in CO2 storage mechanisms [28] [34]. In this way, it is possible to assess CO2 storage in real field process scenarios.

Bibliography

[1] A. Afanasyev, T. Kempka, M. Kühn, and O. Melnik. Validation of the MUFITS reservoir simulator against standard CO2 storage benchmarks and history-matched models of the ketzin pilot site. *Energy Procedia*, 97:395–402, nov 2016.

[2] A. A. Afanasyev. Application of the reservoir simulator MUFITS for 3d modelling of CO2 storage in geological formations. *Energy Procedia*, 40:365–374, 2013.

[3] H. Class, A. Ebigbo, R. Helmig, H. K. Dahle, J. M. Nordbotten, M. A. Celia, P. Audigane, M. Darcis, J. Ennis-King, Y. Fan, B. Flemisch, S. E. Gasda, M. Jin, S. Krug, D. Labregere, A. N. Beni, R. J. Pawar, A. Sbai, S. G. Thomas, L. Trenty, and L. Wei. A benchmark study on problems related to CO2 storage in geologic formations. *Computational Geosciences*, 13(4):409–434, jul 2009.

[4] C. Cooper. A technical basis for carbon dioxide storage. *Energy Procedia*, 1(1):1727–1733, feb 2009.

[5] M. Cusini, B. Fryer, C. van Kruijsdijk, and H. Hajibeygi. Algebraic dynamic multilevel method for compositional flow in heterogeneous porous media. *Journal of Computational Physics*, 354:593–612, feb 2018.

[6] Y. Ding and P. Lemonnier. Use of corner point geometry in reservoir simulation. In *SPE-29933-MS*. SPE, nov 1995.

[7] Z. Duan and R. Sun. An improved model calculating CO2 solubility in pure water and aqueous NaCl solutions from 273 to 533 k and from 0 to 2000 bar. *Chemical Geology*, 193(3-4):257–271, feb 2003.

[8] G. T. Eigestad, H. K. Dahle, B. Hellevang, F. Riis, W. T. Johansen, and E. Øian. Geological modeling and simulation of CO2 injection in the johansen formation. *Computational Geosciences*, 13(4):435–450, aug 2009.

[9] M. Elenius, D. Voskov, and H. Tchelepi. Interactions between gravity currents and convective dissolution. *Advances in Water Resources*, 83:77–88, sep 2015.

[10] H. Emami-Meybodi, H. Hassanzadeh, C. P. Green, and J. Ennis-King. Convective dissolution of CO2 in saline aquifers: Progress in modeling and experiments. *International Journal of Greenhouse Gas Control*, 40:238–266, sep 2015.

[11] J. R. Fanchi. *Shared Earth Modeling*. Elsevier, 2002.

[12] H. Hajibeygi and H. A. Tchelepi. Compositional multiscale finite-volume formulation. *SPE Journal*, 19(02):316–326, nov 2013.

[13] H. Hassanzadeh, M. Pooladi-Darvish, A. M. Elsharkawy, D. W. Keith, and Y. Leonenko. Predicting PVT data for CO2–brine mixtures for black-oil simulation of CO2 geological storage. *International Journal of Greenhouse Gas Control*, 2(1):65–77, jan 2008.

[14] C. Hermanrud, T. Andresen, O. Eiken, H. Hansen, A. Janbu, J. Lippard, H. N. Bolås, T. H. Simmenes, G. M. G. Teige, and S. Østmo. Storage of CO2 in saline aquifers–lessons learned from 10 years of injection into the utsira formation in the sleipner area. *Energy Procedia*, 1(1):1997–2004, feb 2009.

[15] M. HosseiniMehr, J. P. Tomala, C. Vuik, M. A. Kobaisi, and H. Hajibeygi. Projection-based embedded discrete fracture model (pEDFM) for flow and heat transfer in real-field geological formations with hexahedral corner-point grids. *Advances in Water Resources*, 159:104091, jan 2022.

[16] S. T. Ide, K. Jessen, and F. M. Orr. Storage of CO2 in saline aquifers: Effects of gravity, viscous, and capillary forces on amount and timing of trapping. *International Journal of Greenhouse Gas Control*, 1(4):481–491, oct 2007.

[17] R. Juanes, E. J. Spiteri, F. M. Orr, and M. J. Blunt. Impact of relative permeability hysteresis on geological COsub2/substorage. *Water Resources Research*, 42(12), dec 2006.

[18] J. Killough. Reservoir simulation with history-dependent saturation functions. *Society of Petroleum Engineers Journal*, 16(01):37–48, 1976.

[19] K. A. Lie. *An Introduction to Reservoir Simulation Using MATLAB/GNU Octave: User Guide for the MATLAB Simulation Toolbox (MRST).* Cambridge University Press, jul 2019.

[20] B. Metz, O. Davidson, H. De Coninck, M. Loos, and L. Meyer. *IPCC special report on carbon dioxide capture and storage*. Cambridge: Cambridge University Press, 2005.

[21] M. Oak, L. Baker, and D. Thomas. Three-phase relative permeability of berea sandstone. *Journal of Petroleum Technology*, 42(08):1054–1061, aug 1990.

[22] K. Pruess, J. García, T. Kovscek, C. Oldenburg, J. Rutqvist, C. Steefel, and T. Xu. Code intercomparison builds confidence in numerical simulation models for geologic disposal of CO2. *Energy*, 29(9-10):1431–1444, jul 2004.

[23] Q. Shao, S. Matthai, T. Driesner, and L. Gross. Predicting plume spreading during CO2 geo-sequestration: benchmarking a new hybrid finite element–finite volume compositional simulator with asynchronous time marching. *Computational Geosciences*, 25(1):299–323, oct 2020.

[24] N. Spycher and K. Pruess. CO2-h2o mixtures in the geological sequestration of CO2. II. partitioning in chloride brines at 12–100°c and up to 600 bar. *Geochimica et Cosmochimica Acta*, 69(13):3309–3320, jul 2005.

[25] N. Spycher, K. Pruess, and J. Ennis-King. CO2-h2o mixtures in the geological sequestration of CO2. i. assessment and calculation of mutual solubilities from 12 to 100°c and up to 600 bar. *Geochimica et Cosmochimica Acta*, 67(16):3015–3031, aug 2003.

[26] D. A. Steffy, D. A. Barry, and C. D. Johnston. Influence of antecedent moisture content on residual LNAPL saturation. *Journal of Soil Contamination*, 6(2):113–147, mar 1997.

[27] T. N. Tambaria, Y. Sugai, and R. Nguele. Adsorption factors in enhanced coal bed methane recovery: A review. *Gases*, 2(1):1–21, jan 2022.

[28] M. Ţene, S. B. Bosma, M. S. A. Kobaisi, and H. Hajibeygi. Projection-based embedded discrete fracture model (pEDFM). *Advances in Water Resources*, 105:205–216, jul 2017.

[29] C. Teodoriu. Why and when does casing fail in geothermal wells. *Oil, Gas*, 39, 2013.

[30] L. B. van der Meer, C. Hofstee, and B. Orlic. The fluid flow consequences of CO2 migration from 1000 to 600 metres upon passing the critical conditions of CO2. *Energy Procedia*, 1(1):3213–3220, feb 2009.

[31] V. Vilarrasa and J. Rutqvist. Thermal effects on geologic carbon storage. *Earth-Science Reviews*, 165:245–256, feb 2017.

[32] D. V. Voskov and H. A. Tchelepi. Comparison of nonlinear formulations for two-phase multi-component EoS based simulation. *Journal of Petroleum Science and Engineering*, 82-83:101–111, feb 2012.

[33] Y. Wang, C. Vuik, and H. Hajibeygi. Analysis of hydrodynamic trapping interactions during full-cycle injection and migration of CO2 in deep saline aquifers. *Advances in Water Resources*, 159:104073, jan 2022.

[34] Y. Wang, C. Vuik, and H. Hajibeygi. CO2 storage in deep saline aquifers: impacts of fractures on hydrodynamic trapping. *International Journal of Greenhouse Gas Control*, 113:103552, jan 2022.